

Models of particle acceleration and non-thermal emission in colliding-wind binaries



Shubham Joshi
201291466

Submitted in accordance with the requirements for the degree of MPhys and BSc Physics with
Astrophysics

The University of Leeds
School of Physics and Astronomy
April 2022

CONTENTS

- 1 Introduction
 - 1.1 Particle acceleration
 - 1.2 Downstream cooling
 - 1.3 Non-thermal emission
 - 1.4 Report aim and structure
- 2 The model
 - 2.1 Structure and assumptions
 - 2.2 Standard model
- 3 Modelling the non-thermal emission from WR 147
 - 3.1 Parameters
 - 3.2 Varying inclination angle and binary separation
 - 3.3 Varying the magnetic field
 - 3.4 Varying WR mass-loss rate
 - 3.5 Varying O mass-loss rate
 - 3.6 Final model
 - 3.7 WR 147 summary
- 4 Modelling the non-thermal emission from Apep
 - 4.1 Parameters
 - 4.2 Varying inclination angle and binary separation
 - 4.3 Varying the magnetic field
 - 4.4 Varying mass-loss rate
 - 4.5 Final model
 - 4.6 Apep summary
- 5 Conclusions
- 6 Further work
- A CWB structure
- B The Razin effect
- C Alfvén Mach number

Models of particle acceleration and non-thermal emission in colliding-wind binaries

S. Joshi^{1★}¹*School of Physics and Astronomy, Sir William Henry Bragg Building, University of Leeds, Woodhouse, Leeds LS2 9JT, UK*

27 April 2022

ABSTRACT

A recently developed numerical code is presented which models the non-thermal emission from a colliding-wind binary system. The model is applied to WR 147, a particularly wide binary, and Apep, a very luminous binary. An attempt is made to match the model emission of each system with its corresponding observational radio data, with the parameters of the final model from the attempt for each system presented. As parameters are varied, in some instances similar trends are observed for both systems. Reducing binary separation is found to strengthen the non-thermal emission as well as increase the turnover frequency in both systems. And it is also found that in the case of the magnetic flux density, the scaling can be less straightforward. Increasing the mass-loss rate generally strengthens the emission and increases the turnover frequency. Most of the parameters in the final model for both systems are altered to an acceptable degree compared to values obtained from the literature. The paper is concluded by comparing the findings of both systems.

Key words: non-thermal – emission – winds – shock – flux – radio

1 INTRODUCTION

Luminous stars eject rapidly moving, dense, and ionised flows of material referred to as stellar winds (Pittard 2010). In binary systems consisting of early type (hot and massive) stars, these powerful winds can collide at supersonic speeds at a point between the stars, provided the suitable conditions of a wide separation between the stars and a relatively low imbalance between the winds (Pittard et al. 2020). Due to this interaction, stationary opposite facing shocks arise where the winds collide (Dougherty et al. 2003). The shocks are separated by a contact discontinuity, which would be a plane equidistant between both stars if the winds are equal, this configuration is shown in Fig. 1. In the usually observed scenario where the wind from one of the stars is stronger, the contact discontinuity would be a curved surface with the concave side facing the weaker star. In such cases of unequal winds, the location of the wind collision region (WCR) can depend on their history. It is possible that the WCR may remain closer to the originally weaker star having had its weaker wind crushed in the past. The shock heated material in the WCR emits a substantial flux of radio, X-ray, and γ -ray emission. In recent years, numerical simulations modelling this emission have become increasingly complex. Such models allow the opportunity to improve understanding of the various processes of particle acceleration which occur at the WCR.

Colliding-wind binaries (CWBs) are relatively common and consist of early type stars. They typically consist of a Wolf-Rayet star (a massive star at a latter evolution stage where it loses mass at a high rate (Crowther 2007)), and an O type star (a massive, rapidly evolving, hot and blue-white main sequence star (Kroupa 2004)). However, O+O and WR+WR binaries have also been observed. These stars eject winds with terminal velocities of the order of a few

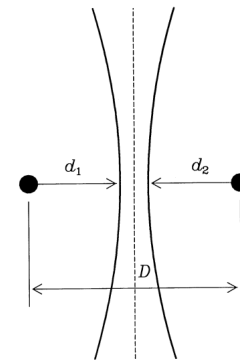


Figure 1. A schematic of the colliding stellar winds in a binary system. The stars are separated by a distance D and the dashed line represents the contact discontinuity, while the solid curved lines represent the shocks (Churchwell et al. 1992).

thousand kilometres per second. They also have very large mass-loss rates. These systems can vary significantly in orbital period, ranging from 1.64 days to 8 years (Stevens et al. 1992). Traditionally, the hydrodynamics of CWBs have been investigated with the aid of two-dimensional models (Pittard 2009). Such models are suitable for wide systems with long orbital periods, where the winds are assumed to be travelling at terminal speeds and orbital effects are unimportant (Pittard & Parkin 2010). An example of such a model is shown in Fig. 2.

CWBs have emerged as suitable candidates for the investigation of the underlying physics of particle acceleration. In comparison to supernova remnants, which are widely used for such studies, CWB

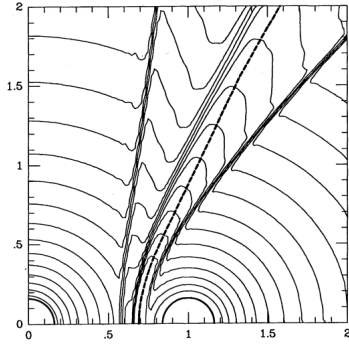


Figure 2. A hydrodynamical simulation of two colliding adiabatic winds. The converging contour lines in between the shocks represent the contact discontinuity and the dashed line represents the momentum balance (Churchwell et al. 1992).

systems provide access to higher mass, radiation and magnetic field energy densities. Numerical simulations developed for CWBs can also be applied to interstellar bow shocks (the shock created as the stellar wind collides with gas and dust in the interstellar medium). Fig. 3 shows how a bow shock is typically formed around a star. In addition, CWBs assist in improving understanding of more complex systems involving colliding winds, such as clusters of massive stars located in the central parsec of the galaxy and young, dense clusters (Pittard & Dougherty 2006).

1.1 Particle acceleration

In CWBs, various processes take place through which particle acceleration occurs and non-thermal emission is produced. Particle acceleration can occur in CWBs through several mechanisms. These include diffusive shock acceleration (DSA), reconnection, and numerous turbulent processes. Types of non-thermal emission include synchrotron emission, Inverse Compton (IC) cooling, relativistic bremsstrahlung, and pion decay (Pittard & Dougherty 2006).

Magnetic field lines can be forced together or become tangled causing them to reconnect at the contact discontinuity and/or within the volume of the WCR. As a result, particle acceleration can occur at these regions. Reconnection plays a meticulous role in particle acceleration, due to the various types of reconnection and the complex magnetic environments associated with this process. In these environments, particles can be accelerated directly through strong electric fields, erratically through the second-order Fermi mechanism, or at the shocks through DSA. In terms of efficiency, DSA is believed to have a marginal advantage over reconnection. Winds are slowed by shocks which bound the WCR and plasma is heated to temperatures of up to 10^7 K or higher. At the shocks, particles can be accelerated to high energies. In some systems these shocks are collision-less and are mediated by magnetic fields as opposed to coulombic particle interactions, a condition which arises in most astrophysical environments. As a result, particles undergo DSA. The concept of particles in astrophysical plasma experiencing diffusive acceleration was first postulated by Enrico Fermi in 1949. He proposed that if particles in interstellar clouds had mostly random directions of motion, the frequency of "head-on" collisions would be greater than the frequency of "head-tail" collisions, leading to a net acceleration which is diffusive in energy. Eventually, it was realised this process could also efficiently occur in shocks within astrophysical

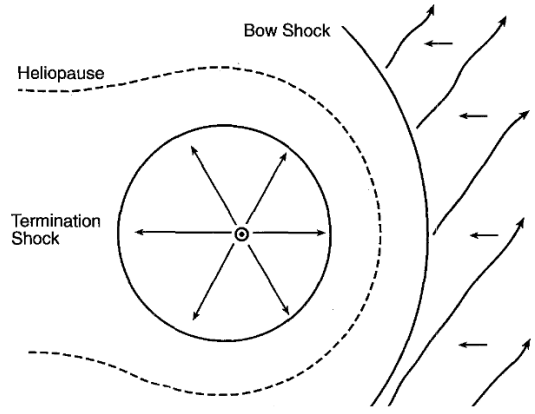


Figure 3. A schematic view of the bow shock formed around the Sun. The sun is located at the centre as a small dot with the orbit of Jupiter around it as a small circle. The arrows pointing towards the top right represent the radial solar wind flow, and the arrows pointing left against the bow shock show the flow of the interstellar medium (Lee 1996).

plasma. DSA involves particles being accelerated by being scattered back and forth across a shock, until the particles gain enough energy to escape the shock as energetic cosmic ray particles. It is a first order Fermi mechanism, which implies that particles gain energy each time they are scattered across the shock, and the energy gained per shock crossing is proportional to the shock velocity. The energy provided to non-thermal particles upstream and downstream of the shock is at the cost of the shock's kinetic energy (Baring 1997). The injection of particles into the DSA process remains to be fully understood. However, it is a problem being tackled through simulations which model the simultaneous acceleration of electrons and ions (Pittard et al. 2021).

In the DSA process, the scattering of particles is caused by magnetic field fluctuations. The interaction of the particles with these fluctuations results in the accelerated particles exerting pressure on the unshocked plasma, located upstream. This results in the development of a shock precursor, which compresses and slows inflowing plasma before it enters the actual shock, referred to as a subshock (Vink & Yamazaki 2014). The subshock can play a role in modifying the shock. As the most energetic particles diffuse further upstream from the subshock, the velocity difference across the subshock is much lower than the classical (unmodified) shock. This results in a reduction of the post shock temperature (Pittard & Dougherty 2006).

Turbulent mechanisms involve non-thermal particles gaining or losing energy depending on the movement of the magnetic field relative to them (whether it is moving towards or away from them). There is an overall increase in momentum due to a surplus of "head-on" collisions. This process is referred to as the second-order Fermi mechanism. The second-order Fermi mechanism is not as fast or efficient as DSA.

1.2 Downstream cooling

Non-thermal electrons experience post shock energy losses due to synchrotron emission, IC emission, relativistic bremsstrahlung, as well as coulombic and adiabatic cooling. IC cooling is dominant for high energy electrons, and low energies are dominated by coulombic cooling. Cooling of non-thermal electrons results in reduced IC and

relativistic bremsstrahlung emission. Non-thermal protons are also subject to cooling although not to a strong degree (Pittard et al. 2020).

1.3 Non-thermal emission

The two main types of continuum emission are thermal and non-thermal emission. Thermal emission is solely dependent on the temperature of the emitter while non-thermal emission involves other processes which do not depend on temperature. An example of thermal emission is black body radiation. And an example of non-thermal radiation is synchrotron radiation (Gulkis & de Pater 2003). In the WCR of CWBs, particles energised by the synchrotron process produce non-thermal radio emission. Other processes such as IC cooling, neutral pion decay, and relativistic bremsstrahlung also produce non-thermal emission in the form of X-rays and γ rays (non-thermal electrons are not energetic enough to produce synchrotron X-ray emission).

Through observations, early type stars have been revealed to be sources of both thermal and synchrotron radio emission. Thermal emission is characterised by a brightness temperature of roughly 10^4 K while synchrotron emission exhibits higher brightness temperatures of more than 10^6 K. Synchrotron emission requires magnetic fields as well as a population of relativistic electrons, which may be accelerated at the shocks bounding the WCR through DSA. Strong observational support exists for the suggestion of a CWB origin for all synchrotron emission observed from Wolf Rayet (WR) stars. The acceleration of non-relativistic particles in a magnetic field produces cyclotron emission. And in the case of relativistic particles, synchrotron emission (also referred to as magneto bremsstrahlung emission) is produced (Dougherty et al. 2003). Electrons moving in a magnetic field follow a circular path. The acceleration electrons experience in this movement results in them emitting photons (Stacy & Vestrand 2003).

IC cooling is a key energy loss mechanism for relativistic electrons in CWBs. One of the first notable models to include the effects of IC cooling was described in Pittard et al. (2006). IC cooling was found to increase significantly with decreasing binary separation. As electrons Inverse Compton scatter, they experience cooling. Anisotropic Compton emission arises through IC scattering, where low energy photons are scattered to higher energies by high energy electrons. The "inverse" term implies it is the electrons which lose energy instead of photons, which is the case in standard Compton scattering.

Emission at γ ray energies can occur through bremsstrahlung if one of the particles is relativistic. As an electron enters the Coulomb field of a positive ion (usually a proton), it is accelerated and loses kinetic energy. Due to conservation of energy, the energy lost is emitted as a photon. This type of emission is referred to as free-free radiation, referring to the electrons being free before and after the emitting of a photon (Stacy & Vestrand 2003).

Fig. 4 shows a density plot with two locations marked in the post-shock flow. Position "A" is located close to the stagnation point (where the local velocity is 0), and position "B" is at an off axis position. At position "A", a lower flow speed maximises exposure time to radiation which has a higher intensity close to the stars, thus IC cooling exerts a stronger influence. At position "B" there are higher energy electrons which produce higher frequency emission, hence synchrotron emission plays a greater role (Pittard et al. 2006).

A pion is any of three subatomic particles, classified as the neutral (π^0), positive (π^+), and negative (π^-) pions. It is a Meson, meaning it consists of a quark and anti-quark. Due to this, they are very unstable, and decay in very short timescales. Neutral pions decay

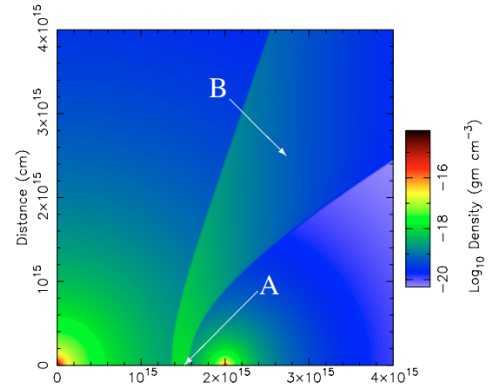


Figure 4. A density plot of a hypothetical CWB model consisting of a WR and O star. The WR star is located at (0,0) (Pittard et al. 2006).

with a mean lifetime of 8.4×10^{-17} seconds, whilst positive and negative pions have a much longer lifetime of 2.6×10^{-8} seconds (Pittard et al. 2021). Neutral pions mostly decay into γ rays, and charged pions generally decay into muons and neutrinos (Grieder 2001). In CWBs, neutral pions are formed as a result of high energy hadronic collisions. The main category of pion decay responsible for non-thermal emission in CWBs is π^0 decay. The majority of radiation from pion decay originates near the apex of the WCR. In π^0 decay, a neutral pion decays into two gamma photons. With a probability of roughly 98.8%, this is the dominant decay mode. The second most common mode is referred to as Dalitz decay (Badala et al. 1994), with a probability of roughly 1.2%. This involves a neutral pion decaying into a γ ray photon and an electron-positron pair (Pittard & Dougherty 2006).

1.4 Report aim and structure

This paper aims to exhibit the results of applying a recently developed numerical model on the CWB systems WR 147 (one of the widest known binaries), and Apep (one of the brightest CWBs to have been observed). The model is described in section 2. In section 3, WR 147 is introduced and the model is applied on it, with comparisons being made between the model radio and observational radio data. Parameters are adjusted in order to provide the best match to the observational radio data. The relation between various parameters and the non-thermal emission is also assessed, and the final model and its parameters are presented. In section 4, the same steps are carried out as in section 3 but for Apep. Final conclusions are drawn for both systems and comparisons are made between them in section 5. Additional potential CWB candidates to model are discussed in section 6. And further details of CWB structure, the Razin effect, and the Alfvén Mach number are noted in a set of appendices.

2 THE MODEL

2.1 Structure and assumptions

The model used has been described in detail in Pittard et al. (2021). The general assumptions are that the WCR is axisymmetric, the winds are travelling at terminal speeds and orbital effects are ignored. Thus, this model is most suitable for wide binaries with long orbital periods, as the winds will have reached terminal speeds, and distortion of the

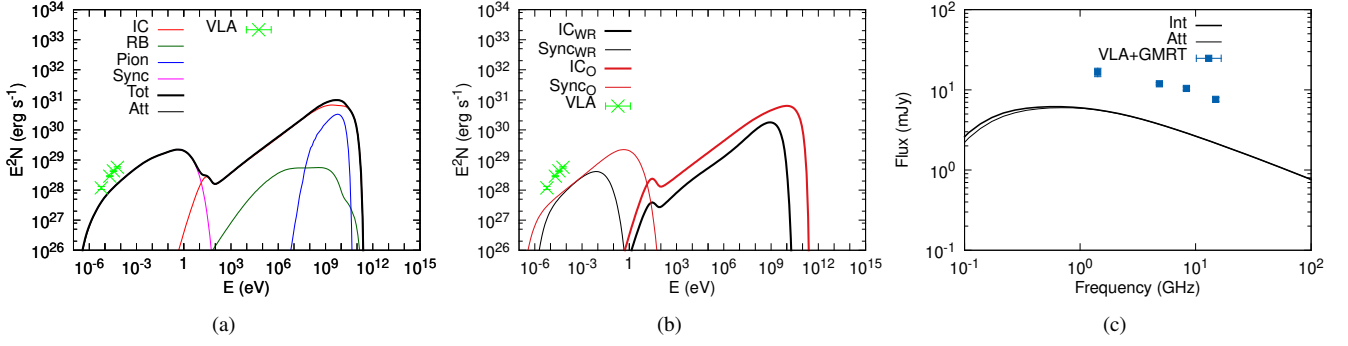


Figure 5. Model spectra for the initial model of WR 147. (a) The model IC, relativistic bremsstrahlung, π^0 decay, synchrotron, total, and attenuated emission are shown with the observed radio data (labelled as "VLA"). (b) The IC and synchrotron emission from the particles accelerated at the WR (back lines) and O (red lines) shock. (c) The intrinsic and attenuated radio emission with the observed radio emission (labelled as "VLA+GMRT").

Table 1. The parameters used in a standard CWB model. Stellar temperature is set to $T = 40000$ K for both stars (Pittard et al. 2020).

Parameter	WR star	O star
\dot{M} ($M_{\odot} \text{ yr}^{-1}$)	2×10^{-5}	2×10^{-6}
v_{∞} (km s^{-1})	2000	2000
L (L_{\odot})	2×10^5	5×10^5

WCR by orbital motion is minimal. It is also assumed that the shocks coincide with the contact discontinuity.

2.2 Standard model

A typical CWB is said to be a WR+O system. Parameters for such a standard system are listed in Table 1. The WR star is referred to as the "primary" star and the O star as the "secondary" star. A reasonably wide stellar separation of $D_{sep} = 2 \times 10^{15}$ cm and a viewing angle of $\phi = 90^\circ$ is assumed. Where the secondary star is in front when $\phi = 0^\circ$, the primary star is in front when $\phi = 180^\circ$, and the system is viewed face on at $\phi = 90^\circ$. Excluding the DSA model, for which the winds are assumed to be pure hydrogen, the rest of the model assumes WC abundances for the WR star and solar abundances for the O star. WC abundances are $X = 0$ (hydrogen), $Y = 0.5$ (helium), and $Z = 0.5$ (metals), and solar abundances are $X = 0.7381$, $Y = 0.2485$, and $Z = 0.0134$. A magnetic flux density of $B_* = 100\text{G}$ is adopted for both stars (Pittard et al. 2021).

3 MODELLING THE NON-THERMAL EMISSION FROM WR 147

The CWB model for WR 147 has been confirmed in numerous publications dating as far back as Moran et al. (1989). WR 147 is very much a typical WR + OB system, being one of the widest such systems in the sky. It is notable for being one of the brightest WR radio sources, and one of the few CWBs to have two spatially resolved regions, one of which emits thermal emission and the other emits synchrotron emission. The southern radio component (coinciding with the WR star) is referred to as WR 147S, and the northern radio component (coinciding with the O star) is referred to as WR 147N, which is the non-thermal component (Churchwell et al. 1992). The system is located 650 pc away, making it one of the nearer known CWBs (Dougherty et al. 2003).

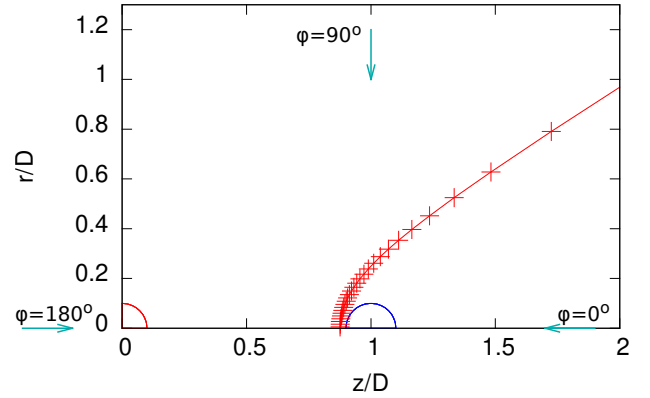


Figure 6. The position of the contact discontinuity of WR 147. The red and blue circles represent the primary and secondary star respectively. The labelled arrows show the perspective from different viewing angles.

3.1 Parameters

To produce emission data, the model requires a number of parameters associated with the CWB system of choice. Extensive literature was consulted to obtain a reliable set of initial parameters for WR 147. As per Dougherty et al. (2003), mass-loss rates of $\dot{M}_{WR} = 2 \times 10^{-5} M_{\odot} \text{ yr}^{-1}$ and $\dot{M}_O = 3.8 \times 10^{-7} M_{\odot} \text{ yr}^{-1}$ were adopted for the WR and O star respectively. Found in the same publication, wind speeds were set to $v_{\infty WR} = 9.5 \times 10^7 \text{ cm s}^{-1}$ and $v_{\infty O} = 1.0 \times 10^8 \text{ cm s}^{-1}$. Stellar luminosities were calculated using the luminosity equation

$$L = 4\pi R^2 \sigma T^4 \quad (1)$$

where L is the luminosity, R is the stellar radius, σ is the Stefan-Boltzmann constant, and T is the stellar temperature. Using this equation, values of $L_{WR} = 1.4 \times 10^5 L_{\odot}$ and $L_O = 4.3 \times 10^4 L_{\odot}$ were obtained. A WR temperature of $T_{WR} = 39800$ K was used as per Hamann et al. (2006). And an O temperature of $T_O = 29000$ K was set found in Williams et al. (1997). A WR radius of $R_{WR} = 7.94 R_{\odot}$ from Hamann et al. (2006) and an O radius of $R_O = 8.21 R_{\odot}$ from Silaj et al. (2014) was obtained. Wind temperatures of both stars were assumed to be 10000 K. WR abundances of $X = 0.09$, $Y = 0.89$, and $Z = 0.016$ were used, and the O abundances were set to solar values

of $X = 0.7381$, $Y = 0.2485$, and $Z = 0.0134$ as per [Dougherty et al. \(2003\)](#). The separation was calculated using $D_{sep} = 415/\cos i$ AU, where $i = 90 - \phi$. The inclination angle remains yet to be particularly well constrained. A starting value of $\phi = 30^\circ$ was used to achieve a value of i which would give a suitably wide separation. Using $i = 60^\circ$ gave a separation of $D_{sep} = 1.24 \times 10^{16}$ cm. A magnetic flux density of $B_* = 10$ G was used for both stars as a suitable starting point, due to the magnetic field strength in CWBs being typically very uncertain. And the filling factor was set to $f = 1.0$ as the winds are assumed to be smooth (the same assumption made for WR 146 in [Pittard et al. \(2021\)](#)).

Fig. 6 displays the structure of the CD corresponding to the starting parameters. Using the previously mentioned parameters, model spectra of the emission were obtained, shown in Fig. 5. Synchrotron emission dominates at $E \lesssim 1$ eV while IC emission dominates at $E \gtrsim 100$ eV. And π^0 decay emission becomes comparable in strength to the IC between 10^9 and 10^{10} eV. In its entire range, relativistic bremsstrahlung emission appears a few orders of magnitude weaker than the IC emission. It can be seen in Fig. 5b that the shock of the O star is a larger contributor to the non-thermal emission, exceeding the emission from the WR shock in both the IC and synchrotron processes. A slight "bump" roughly between 10 and 100 eV is observed in the IC emission from particles accelerated at both shocks. A similar result was present in Figure 9 in [Pittard et al. \(2021\)](#) for the standard model. It was attributed to electrons experiencing downstream cooling resulting in a particle distribution peak. The outcome in Fig. 5b was likely due to this mechanism. Without the presence of downstream cooling, this "bump" would not be present, as the downturn in flux would be smoother. Fig. 5c displays the model data compared to observational radio data obtained from [Churchwell et al. \(1992\)](#) and [Contreras & Rodriguez \(1999\)](#). A downturn in flux occurs at slightly below 1 GHz, this frequency is referred to as the turnover frequency. The downturn in emission is usually caused by a combination of the Razin effect and free-free absorption (an electron absorbing radiation as it passes an ion) ([Dougherty et al. 2003](#)). Leading up to the turnover frequency, there is some visible attenuation which weakens as free-free absorption becomes negligible ([Pittard & Dougherty 2006](#)). The initial parameters do not provide a good match for the VLA data, as the model radio emission is too weak, suggesting that parameters need to be altered in order to improve the fit.

3.2 Varying inclination angle and binary separation

Having obtained results for the inclination angle set to $\phi = 30^\circ$, plots were obtained for $\phi = 90^\circ$ and $\phi = 5^\circ$, which gave separations of $D_{sep} = 6.21 \times 10^{15}$ cm and $D_{sep} = 7.21 \times 10^{16}$ cm respectively. These values gave a suitably large range of separation which allowed to judge the effect of varying the inclination angle and separation with more ease. Fig. 7 shows these results.

The model spectra for $\phi = 90^\circ$ appear somewhat similar to the plots for the initial value of $\phi = 30^\circ$. From Fig 7a, it can be seen that IC and Synchrotron emission dominate at a similar range of E , while relativistic bremsstrahlung emission is again weaker by a few orders of magnitude in comparison to the IC emission. The notable contrast is in the π^0 decay emission, which occupies a similar range of E but appears to match and even marginally exceed the IC emission for a narrow range located roughly between 10^9 and 10^{10} eV. There are also similarities in the plot showing the emission from each shock. Fig. 7b confirms that the O shock remains a stronger contributor to the IC and synchrotron emission. Shown in 7c, the turnover frequency and the general shape of the curve remain somewhat similar. A larger visible

difference between the intrinsic and attenuated emission signifies a stronger role played by free-free and photon-photon absorption. The model is once again not a good fit for the observational data.

In contrast to $\phi = 90^\circ$, the plots for $\phi = 5^\circ$ appear noticeably different to $\phi = 30^\circ$. Fig. 7d shows that synchrotron emission dominates at a familiar range of $E \lesssim 1$ eV. However, the emission weakens at $E \gtrsim 0.1$ eV by less than an order of magnitude. IC emission begins to dominate at a slightly lower energy at $E \gtrsim 10$ eV, and appears fainter by less than an order of magnitude in comparison to Fig. 5a. Relativistic bremsstrahlung emission remains a few orders of magnitude weaker than the IC emission while π^0 decay emission has reduced by roughly an order of magnitude. As a result, the overall dominance of IC emission has grown at the highest energies ($E \gtrsim 10^6$ eV). The total non-thermal emission is visibly reduced. As seen in Fig. 7e, there is a noticeable change in the synchrotron and IC emission from each shock. While in previous plots the O shock was a stronger contributor to both the synchrotron and IC emission, it is now a more complex case. The synchrotron emission is dominated by the WR shock roughly between 10^{-4} and 1 eV, while the O shock dominates the vast majority of the IC emission. The turnover frequency (as seen in Fig. 7f) appears lower than both $\phi = 30^\circ$ and $\phi = 90^\circ$. The model data evidently does not provide a good fit, as the model emission remains too weak.

Fig. 7g shows the total non-thermal emission for $\phi = 5^\circ$, $\phi = 30^\circ$, and $\phi = 90^\circ$ plotted together, while Fig. 7h shows the corresponding radio data. The highest non-thermal emission is given by $\phi = 90^\circ$, followed by $\phi = 30^\circ$, and $\phi = 5^\circ$. The corresponding separation values in the same order are $D_{sep} = 6.21 \times 10^{15}$ cm, $D_{sep} = 1.24 \times 10^{16}$ cm, and $D_{sep} = 7.21 \times 10^{16}$ cm. There is no clear proportionality between the separation and synchrotron emission at $E \lesssim 0.1$ eV. However, above 0.1 eV the synchrotron emission appears to scale inversely with separation. As both stars move closer, the WCR is surrounded by increasingly dense gas as it lies closer to each star, and the thermal energy density in the WCR is increased. As a result, the magnetic field is stronger and particles are accelerated to higher energies. Thus, synchrotron emission is stronger ([Dougherty et al. 2003](#)). As the surrounding gas becomes more dense, the stronger role played by free-free absorption and the Razin effect may be responsible for the low energy ($E \lesssim 0.1$ eV) synchrotron emission not increasing with decreasing separation. This is supported by [Pittard et al. \(2006\)](#) where it was found that such processes may result in the observed synchrotron emission decreasing with a lower separation. The IC, relativistic bremsstrahlung, and π^0 decay emission are also found to scale inversely with separation, this is consistent with [Pittard et al. \(2020\)](#). The π^0 decay emission in particular seems to benefit from a decreasing separation, relative to the other processes, also seen in [Pittard et al. \(2021\)](#). It is clear from Figs 5a, 7a, and 7d that at closer separations, γ rays from π^0 decay make a growing contribution to the high energy emission. This is due to the increased density of the post-shock gas, as a result of which high energy hadronic collisions from which neutral pions are created occur at a more frequent rate ([Pittard & Dougherty 2006](#)). From Figs 5c, 7c, and 7f, it is evident that the attenuation of the radio emission is stronger with a lower separation, a finding also present in [Dougherty et al. \(2003\)](#). This is likely due to the increased prominence of free-free absorption with the increasing gas density as the separation is lowered. To summarise, it can be deduced that the total non-thermal emission and turnover frequency scale inversely with binary separation, which is the typical outcome for a CWB system, and consistent with [Dougherty et al. \(2003\)](#).

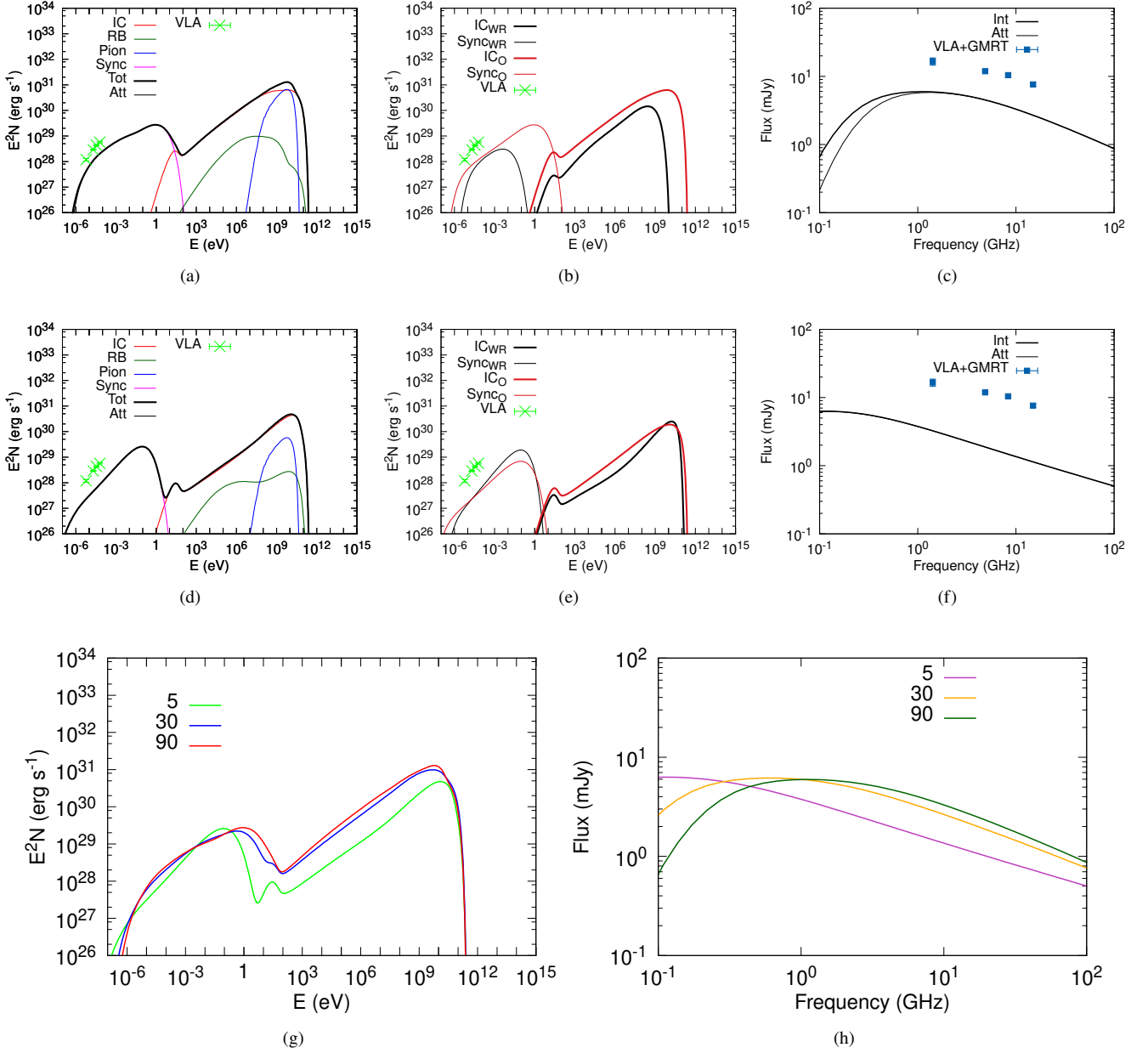


Figure 7. The dependence of the non-thermal emission on the inclination. Panels (a), (b), and (c) show the emission for $\phi = 90^\circ$ while panels (d), (e), and (f) represent the plots for $\phi = 5^\circ$. Panel (g) shows the total non-thermal emission for all three values (including the initial value) of ϕ while (h) exhibits the intrinsic radio emission for the same values.

3.3 Varying the magnetic field

Fig. 8 shows the effect of adjusting magnetic flux density on the resulting non-thermal emission. Shown in, Figs 8a, 8b, and 8c is the emission for both stars set to $B_* = 1G$. In Fig. 8a, one of the notable features is a significant reduction in emission roughly between 0.1 and 1 eV. The synchrotron and IC emission both appear to have reduced, by a factor ranging from less than one to a few orders of magnitude at different energies, dominating at the expected energies. Relativistic bremsstrahlung emission remains a few orders of magnitude weaker than the IC. IC emission dominates at most of the high energies with the exception of a narrow range located around 10^9 eV, where π^0 decay emission is dominant. Compared

to the plot made with the initial parameters (Fig. 5b), it can be seen in Fig. 8b that the synchrotron emission from both shocks is reduced, with the emission from the WR shock having weakened by a wider margin. The synchrotron emission from the O shock is around an order of magnitude weaker while the corresponding WR shock is a few orders of magnitude fainter. As a result, the O shock dominates the synchrotron emission to a higher degree. The IC emission continues to be dominated by the O shock, albeit to a slightly lesser degree than what was seen with the initial parameters. The O shock now only clearly dominates the IC emission at $E \lesssim 10^3$ eV and $E \gtrsim 10^8$ eV. Seen in Fig 8c, the turnover frequency is lower, and the model radio emission is weaker compared to Fig. 5c by less than

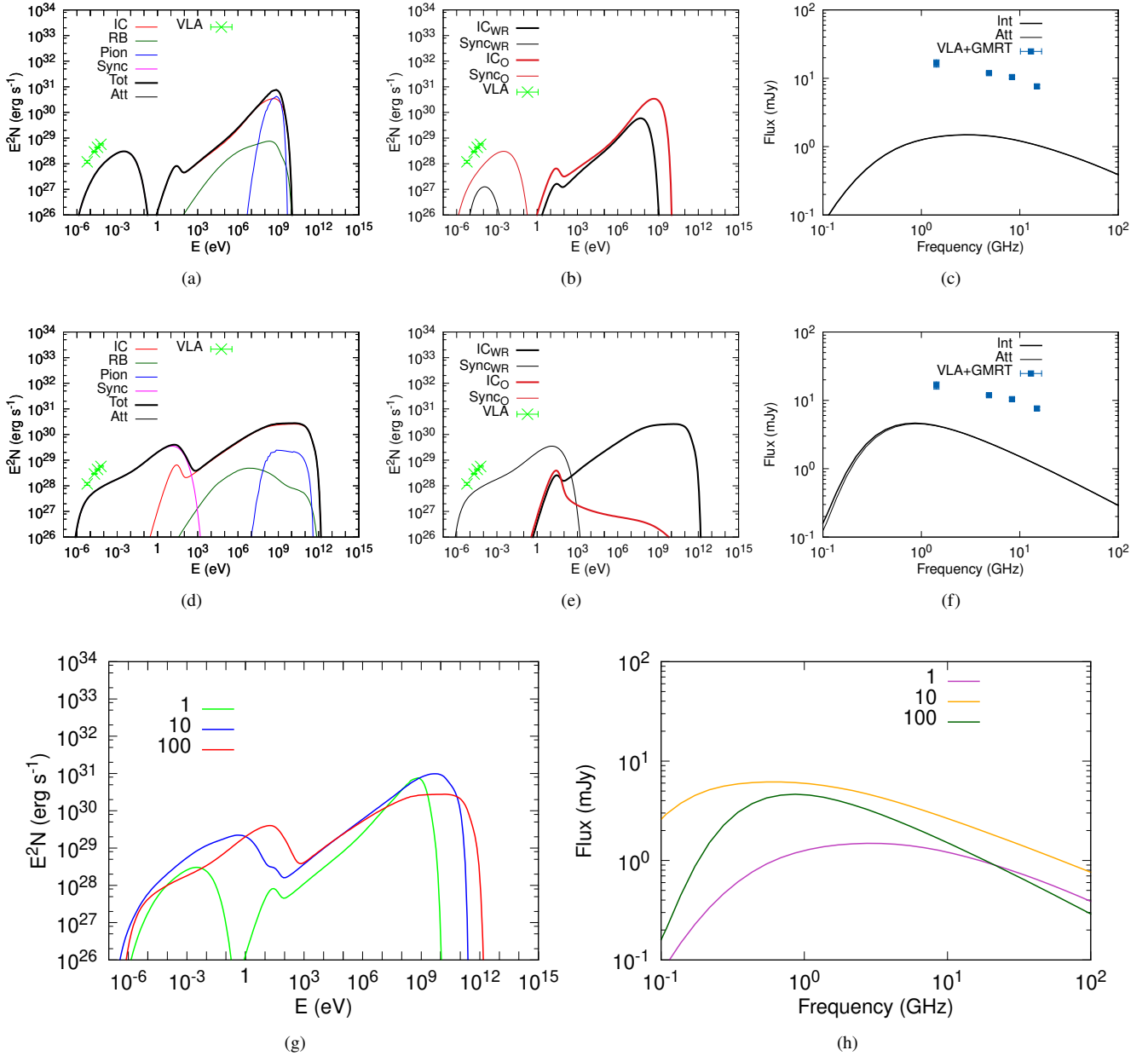


Figure 8. The dependence of the non-thermal emission on the magnetic flux density. Panels (a), (b), and (c) show the emission for $B_* = 1G$ while panels (d), (e), and (f) represent the plots for $B_* = 100G$. Panel (g) shows the total non-thermal emission for all three values (including $B_* = 10G$) of B_* while (h) exhibits the intrinsic radio emission for the same values.

an order of magnitude, and thus not a good fit for the observational data.

Shown in, Fig. 8d, Fig. 8e, and Fig. 8f is the emission for $B_* = 100G$. In Fig. 8d, the total non-thermal emission is visibly higher than what was seen for $B_* = 1G$, and somewhat similar to the plot obtained with the initial value of $B_* = 10G$. Synchrotron and IC emission dominate at the familiar energies (synchrotron emission dominating low energies while IC dominates high energies). And relativistic bremsstrahlung emission remains a few orders of magnitude weaker than the IC emission. It is clear that the contribution of π^0 decay has reduced in comparison to Fig. 5a, with the emission weakening by around an order of magnitude. This is in contrast with what

was seen in Fig 8a, where the contribution of π^0 decay had grown. Significant changes are observed in Fig. 8e, where it can be seen that the synchrotron emission from the O shock has reduced by several orders of magnitude. It can be assumed that the Synchrotron emission is now almost entirely generated at the WR shock. While not to the same degree, the IC emission from the O shock has also weakened by a considerable margin, lowering by at least a few orders of magnitude or more at $E \gtrsim 10^3$ eV. It can be deduced the WR shock strongly dominates the IC emission. As seen in Fig. 8f, the turnover frequency remains lower compared to the initial value of $B_* = 10G$. And the model radio data is not a good fit for the observational radio data.

Fig. 8g shows the total non-thermal emission for $B_* = 1G$, $B_* =$

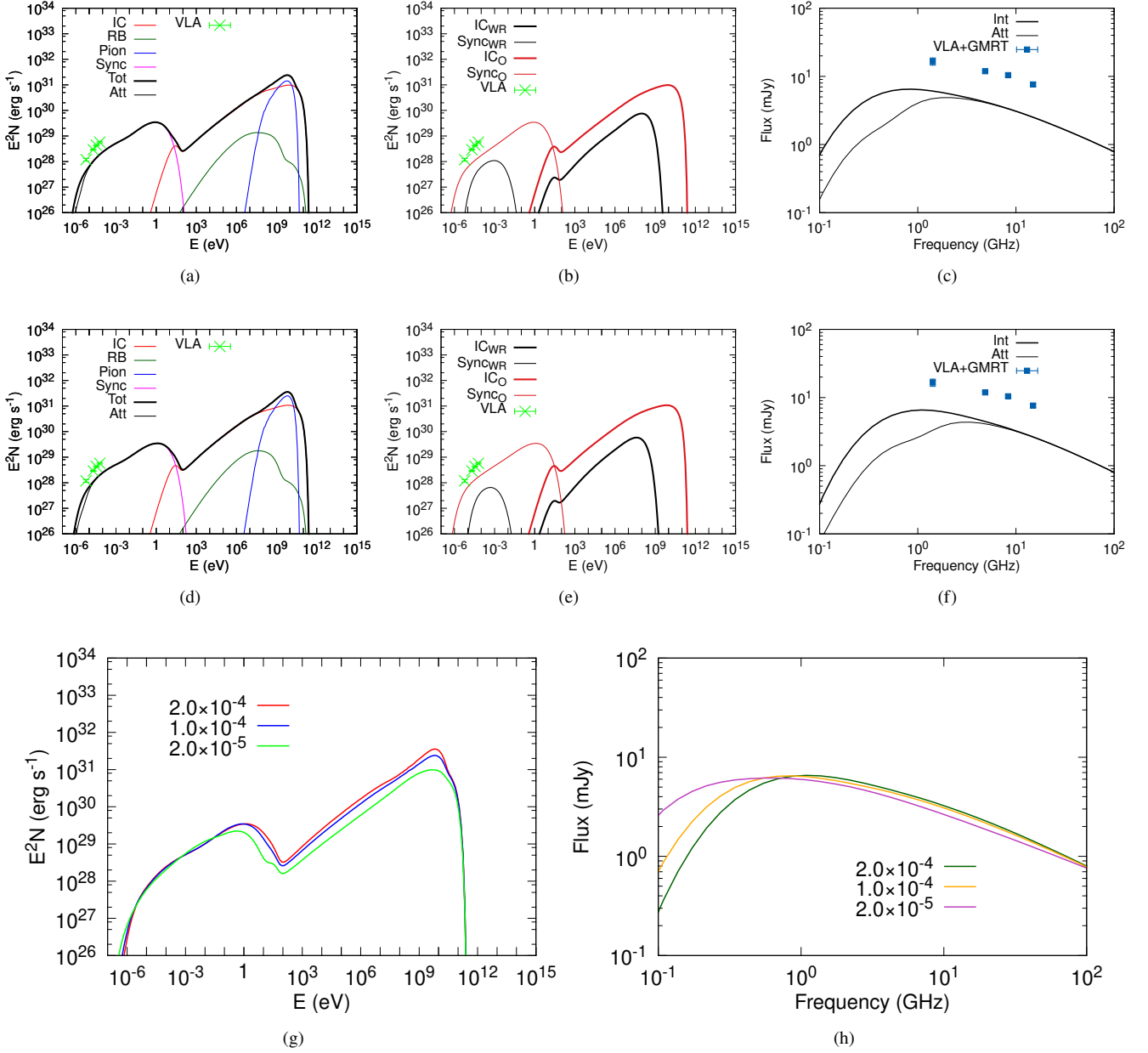


Figure 9. The dependence of the non-thermal emission on the magnetic flux density. Panels (a), (b), and (c) show the emission for $\dot{M}_{WR} = 1.0 \times 10^{-4} M_{\odot} \text{yr}^{-1}$ while panels (d), (e), and (f) represent the plots for $\dot{M}_{WR} = 2.0 \times 10^{-4} M_{\odot} \text{yr}^{-1}$. Panel (g) shows the total non-thermal emission for all three values of \dot{M}_{WR} (including the initial value) while (h) exhibits the intrinsic radio emission for the same values.

10G, and $B_* = 100\text{G}$ plotted together. While Fig. 8h shows the corresponding radio data. The total non-thermal emission appears to be lowest at $B_* = 1\text{G}$, and the emission for $B_* = 10\text{G}$ and $B_* = 100\text{G}$ is higher, sharing a somewhat similar emission spectrum. At higher energies ($E \gtrsim 10^8\text{ eV}$), the emission peak is stronger for $B_* = 10\text{G}$. From figs 5a, 8a, and 8d, it is evident synchrotron, IC, and relativistic bremsstrahlung emission have a complex dependency on B_* . While the relativistic bremsstrahlung emission appears altered to a lesser degree, notable variations are visible in both the synchrotron and IC emission. As B_* is increased from 1G to 10G, the synchrotron emission rises in strength by roughly an order of magnitude. But as B_* is further increased to 100G, this trend does not continue, as

while the synchrotron emission increases at high energies (between 1 and 1000 eV), it weakens at the rest of the spectrum ($E \lesssim 1\text{ eV}$). A similar finding is present for the IC emission, where the emission increases from $B_* = 1\text{G}$ to $B_* = 10\text{G}$, but as B_* is further increased to 100G, the emission only strengthens at the highest energies ($E \gtrsim 10^{11}\text{ eV}$), while weakening at the rest of the spectrum (in this case mainly between 10^6 and 10^{11} eV). This is likely due to conflicting effects between the particle acceleration efficiency increasing with the Alfvén Mach number (a measure of strength of the magnetic field), and decreasing with the magnetic field as the maximum proton energy lowers due to a high energy turnover (Pittard et al. 2021) caused by Alfvén wave heating (Ellison et al. 2004). From Figs 5b,

8b, and 8e, it is apparent that these conflicting effects play a stronger role in the O shock, whereas synchrotron and IC emission from the WR shock appears to scale directly with B_* . This is likely due to the maximum non-thermal proton momentum being higher in the WR shock as a result of the distance between the WR shock and WR star being larger than the distance between the O shock and O star (Pittard et al. 2021). In contrast with the other processes, the π^0 decay emission appears to scale inversely with B_* , this is consistent with Pittard & Dougherty (2006) where it was stated that π^0 decay flux is directly proportional to the magnetic field strength. It can be seen in Fig. 8h that the turnover frequency also has no clear scaling with B_* . The expected result is for the turnover frequency to scale inversely with the magnetic field (Pittard et al. 2021). This suggests the dependence of the turnover frequency on B_* is reduced compared to a typical CWB, indicating a potentially weaker role played by the Razin effect. An appropriate fit for the observational data is not provided by any of the values. It can be concluded that the non-thermal emission scales in a complex manner with the magnetic flux density.

3.4 Varying WR mass-loss rate

Fig. 9 shows the effect of adjusting the mass-loss rate of the primary (WR) star. Shown in Figs 9a, 9b, and 9c are the emission plots for the mass-loss rate set to $\dot{M}_{WR} = 1.0 \times 10^{-4} M_{\odot} \text{yr}^{-1}$. As observed with the initial parameters ($\dot{M}_{WR} = 2.0 \times 10^{-5} M_{\odot} \text{yr}^{-1}$), synchrotron emission dominates at $E \lesssim 1$ eV, and IC emission mostly dominates at $E \gtrsim 100$ eV. Similarity also lies in the relativistic bremsstrahlung emission, as it remains a few orders of magnitude weaker than the IC emission. A notable change is seen in the π^0 decay emission, which dominates in a narrow range roughly between 10^9 and 10^{10} eV. The synchrotron emission from the O shock, as seen in Fig. 9b, seems mostly unaltered. However, the synchrotron emission from the WR shock appears to have weakened by around an order of magnitude. As a result, the O shock is more dominant in the total synchrotron emission. There is not as much of a significant change visible in the IC emission from each shock, with the only notable feature being the O shock becoming slightly more dominant between 10^3 and 10^9 eV. While the intrinsic radio emission appears somewhat similar (as seen in Fig. 9), the attenuated emission is noticeably lower. This may be attributed to the increased prominence of free-free absorption. It is clear the model radio data is not a good fit for the observational data.

Shown in Figs 9d, 9e, and 9f, are the emission plots for $\dot{M}_{WR} = 2.0 \times 10^{-4} M_{\odot} \text{yr}^{-1}$. The plots appear to resemble what was obtained for $\dot{M}_{WR} = 1.0 \times 10^{-4} M_{\odot} \text{yr}^{-1}$. Synchrotron and IC emission dominate at similar energy ranges, while relativistic bremsstrahlung emission remains a few orders of magnitude weaker than the IC. A subtle difference lies in the π^0 decay emission, which now dominates at a wider energy range between just below 10^9 eV and 10^{10} eV. The Synchrotron and IC emission from each shock, as seen in Fig. 9e, also appear mostly unchanged (compared to the plots for $\dot{M}_{WR} = 1.0 \times 10^{-4} M_{\odot} \text{yr}^{-1}$). The O shock remains the stronger contributor to both emission types. Further likeness is observed in the radio emission plot shown in Fig. 9f, in the shape of the spectrum as well as the level of attenuated emission. And thus, this model radio data is also not a good fit for the observational data.

Fig. 9g shows the total non-thermal emission for $\dot{M}_{WR} = 2.0 \times 10^{-4} M_{\odot} \text{yr}^{-1}$, $\dot{M}_{WR} = 1.0 \times 10^{-4} M_{\odot} \text{yr}^{-1}$, and $\dot{M}_{WR} = 2.0 \times 10^{-5} M_{\odot} \text{yr}^{-1}$ plotted together. While Fig. 9h shows the corresponding radio plots. The total non-thermal emission appears to scale with the WR mass-loss rate at $E \gtrsim 0.1$ eV. This can be attributed

to the increased mass-loss rate straightforwardly providing a greater amount of energy in the winds for particle acceleration to occur and non-thermal emission to be produced (Pittard et al. 2020). At the rest of the spectrum there is no clear proportionality. As the density of the gas surrounding the WCR increases with the mass-loss rate, the stronger role played by free-free absorption and the Razin effect at lower energies may be responsible for this outcome (Dougherty et al. 2003). From Figs 5a, 9a, and 9d, it can be seen that the relativistic bremsstrahlung emission scales subtly with the mass-loss rate, likely due to the increased mass-loss rate providing a larger population of non-thermal electrons (Pittard & Dougherty 2006). The aforementioned figures also show that increasing the WR mass-loss rate strengthens the π^0 decay emission. This can be attributed to the increased rate of hadronic collisions as the post-shock gas density is increased, creating more neutral pions (Pittard & Dougherty 2006). From Figs 5c, 9c, and 9f, it is clear that the level of attenuation of the radio flux scales directly with the WR mass-loss rate. The probable cause is the increased gas density due to which free-free absorption is more prominent. Fig. 9h, it can be deduced that increasing the WR mass-loss rate also increases the turnover frequency. An appropriate fit for the observational radio data remains yet to be achieved by any of the aforementioned values.

3.5 Varying O mass-loss rate

Fig. 10 shows the effect of adjusting the mass-loss rate of the secondary (O) star. Shown in Fig. 10a, Fig. 10b, and Fig. 10c are the emission plots for the mass-loss rate set to $\dot{M}_O = 1.0 \times 10^{-6} M_{\odot} \text{yr}^{-1}$. The overall non-thermal emission is noticeably higher. Synchrotron and IC emission dominate at the typical energies while the relativistic bremsstrahlung emission has grown in strength by an order of magnitude, compared to Fig. 5a, although it remains roughly a few orders of magnitude weaker than the IC. From the same figure, it is clear π^0 decay emission becomes comparable in strength between 10^9 and 10^{10} eV. Compared to Fig. 5b, the O shock dominates the synchrotron and IC Emission to a similar degree. And the model radio data (Fig. 10), is the first instance examined so far of providing an appropriate fit for the observational radio data of WR 147.

Shown in Figs 10d, 10e, and 10f are the emission plots for the mass-loss rate set to $\dot{M}_O = 3.8 \times 10^{-6} M_{\odot} \text{yr}^{-1}$. The spectra appear somewhat similar to what was obtained for $\dot{M}_O = 1.0 \times 10^{-6} M_{\odot} \text{yr}^{-1}$. As usually observed, Synchrotron emission dominates at lower energies whilst IC emission dominates at higher energies. The prominence of relativistic bremsstrahlung has grown further compared to Fig. 10a, being less than an order of magnitude fainter than the IC in parts of the spectrum. An increase is also noticeable in the π^0 decay emission, which slightly eclipses the IC emission for a very narrow range around 10^9 eV. In contrast, Fig. 10e appears mostly alike to Fig. 10b, aside from the contribution to the IC emission from the WR shock growing marginally. With the aid of Fig. 10f, it can be deduced the model emission is too strong to be a good fit for the observational data.

Fig. 10g shows the total non-thermal emission for $\dot{M}_O = 3.8 \times 10^{-6} M_{\odot} \text{yr}^{-1}$, $\dot{M}_O = 1.0 \times 10^{-6} M_{\odot} \text{yr}^{-1}$, and $\dot{M}_O = 3.8 \times 10^{-7} M_{\odot} \text{yr}^{-1}$ plotted together. While Fig. 10h shows the corresponding radio plots. As seen with the WR mass-loss rate, the non-thermal emission scales with the O mass-loss rate, this can also assumed to be driven by the higher amount of energy provided by greater mass-loss rate. However, comparing Fig. 9g and Fig. 10g, it is clear that the O mass-loss rate has a greater influence on the non-thermal emission. This is likely due to the WCR lying closer to the O star, and relatively far from the WR star, as a result

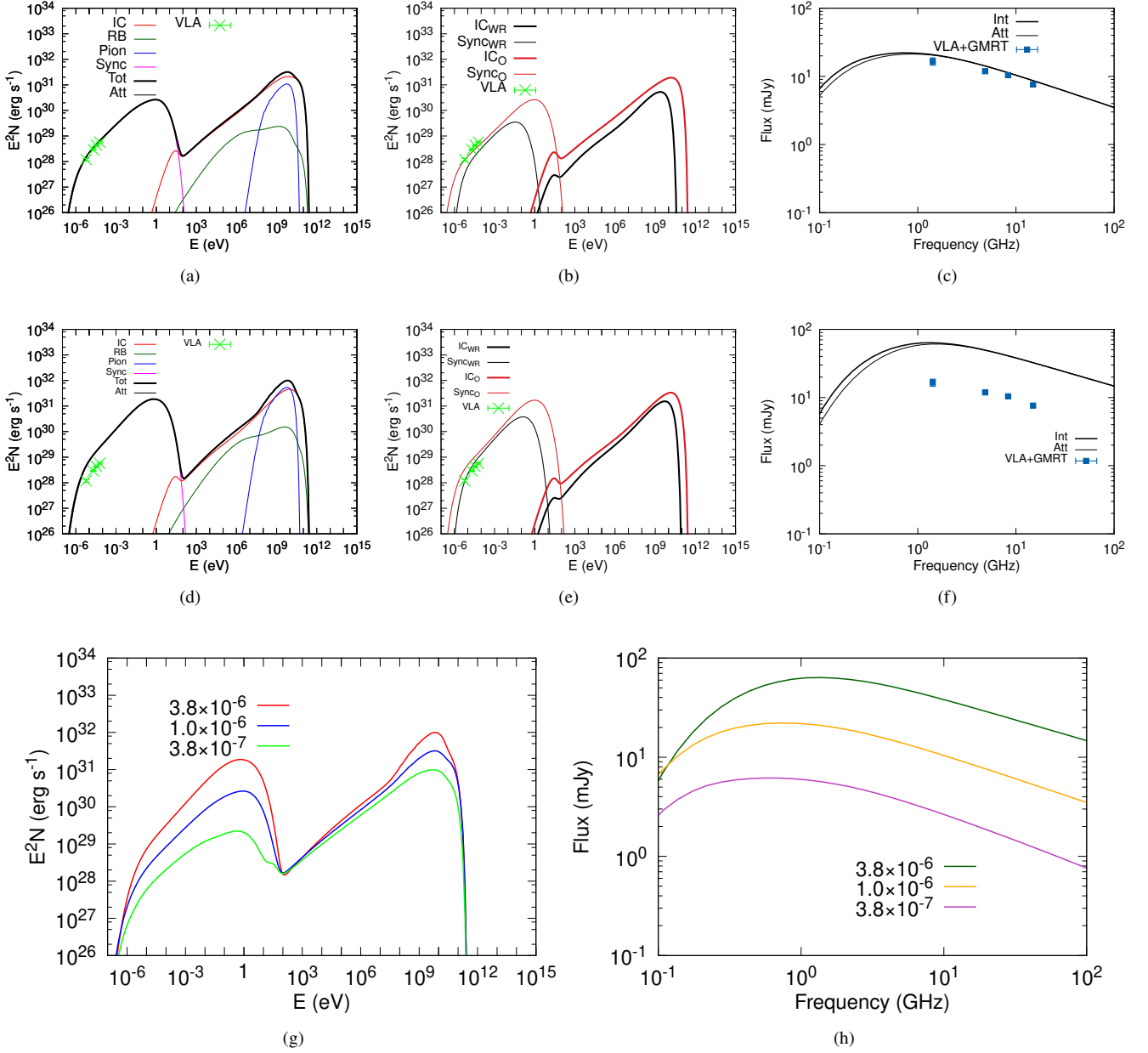


Figure 10. The dependence of the non-thermal emission on the O mass-loss rate. Panels (a), (b), and (c) show the emission for $\dot{M}_O = 1.0 \times 10^{-6} M_\odot$ while panels (d), (e), and (f) represent the plots for $\dot{M}_O = 3.8 \times 10^{-6} M_\odot$. Panel (g) shows the total non-thermal emission for all three values of \dot{M}_O (including the initial value) while (h) exhibits the intrinsic radio emission for the same values.

of which increasing the WR mass-loss rate has a relatively small effect compared to the O mass-loss rate. It is also clear that the non-thermal emission scales directly with the O mass-loss rate at all energies, unlike what was observed with the WR mass-loss rate. This suggests that at lower energies, free-free absorption and the Razin effect do not have as much influence in the O shock compared to the WR shock. From Figs 5a, 10a, and 10d, it is apparent that the relativistic bremsstrahlung emission scales directly with the mass-loss rate, which can be attributed to the larger available population of non-thermal electrons (Pittard & Dougherty 2006). The O mass-loss rate appears to have a stronger influence on this particular emission, suggesting the O star's winds play a greater role

in providing non-thermal electrons to undergo the bremsstrahlung process. As seen with the WR star, increasing the mass-loss rate also strengthens the π^0 decay emission in particular, relative to the other processes. This is evident by the increasingly pronounced peak in the emission (located roughly at 10^{10} eV) with higher mass-loss rates. As with the WR mass-loss rate, this is also likely due to the increased rate of hadronic collisions as a consequence of the higher gas density. Similarity also lies in Fig. 10h, where the turnover frequency continues to scale with the mass-loss rate. An appropriate fit for the observational data was found with a mass-loss rate of $\dot{M}_O = 1.0 \times 10^{-6} M_\odot \text{yr}^{-1}$.

Table 2. The parameters used in the final model of WR 147. An inclination angle of $\phi = 30^\circ$ implies a binary separation of $D_{sep} = 1.24 \times 10^{16} \text{ cm}$. And the distance is set to 0.65 kpc.

Parameter	WR star	O star
$\dot{M} (M_\odot \text{ yr}^{-1})$	2×10^{-5}	1×10^{-6}
$v_\infty (kms^{-1})$	950	1000
$L (L_\odot)$	1.4×10^5	4.3×10^4
$T_{eff} (K)$	39 800	29 000
$R_* (R_\odot)$	7.94	8.21
$T_{wind} (K)$	1 000	1 000
X	0.09	0.7381
Y	0.89	0.2485
Z	0.016	0.0134
$B_* (G)$	10	10
v_{rot}/v_∞	0.1	0.1
f	1.0	1.0

3.6 Final model

In an attempt to achieve a suitable fit for the observational radio data of WR 147, many alterations were made to various parameters. These included the inclination angle (ϕ), binary separation (D_{sep}), magnetic flux density (B_*), as well as the mass-loss rates (\dot{M}_{WR} and \dot{M}_O). Compared to the initial model described in Section 3.1, the vast majority of the parameters remains unchanged in the final model, with the exception being the mass-loss rate of the O star. It was found that setting the value to $\dot{M}_O = 1.0 \times 10^{-6} M_\odot \text{ yr}^{-1}$ gave a suitable fit for the observational data. While this value is more than double the initial mass-loss rate of $\dot{M}_O = 3.8 \times 10^{-7} M_\odot \text{ yr}^{-1}$, in the context of CWB systems, it is a more than acceptable deviation. Many parameters of these systems, including the mass-loss rates, are not particularly well constrained, allowing for some degree of flexibility.

3.7 WR 147 summary

Modelling the non-thermal emission of the wide binary WR 147 has been carried out. The inclination angle (ϕ), magnetic flux density (B_*), and mass-loss rates (\dot{M}_{WR} and \dot{M}_O) were all adjusted to investigate how these parameters influence the non-thermal emission produced. The total non-thermal emission and turnover frequency are found to scale inversely with the separation, with the π^0 decay emission strengthening in particular relative to the other processes with a decreasing separation. The non-thermal emission is found to have a more complex dependency on the magnetic flux density, due to conflicting effects within the WCR as B_* is increased. While the turnover frequency also scales in a complex manner with B_* . The π^0 decay emission and synchrotron emission from the WR shock in particular are found to benefit in strength from a higher value of B_* . Altering the mass-loss rates of both stars yielded the matching outcome of the non-thermal emission and turnover frequency scaling directly with the mass-loss rate, with the emission scaling more effectively with \dot{M}_O than with \dot{M}_{WR} . The parameters remain unchanged aside from \dot{M}_O in the final model, with an alteration which can be considered acceptable. The final model parameters are listed in Table 2.

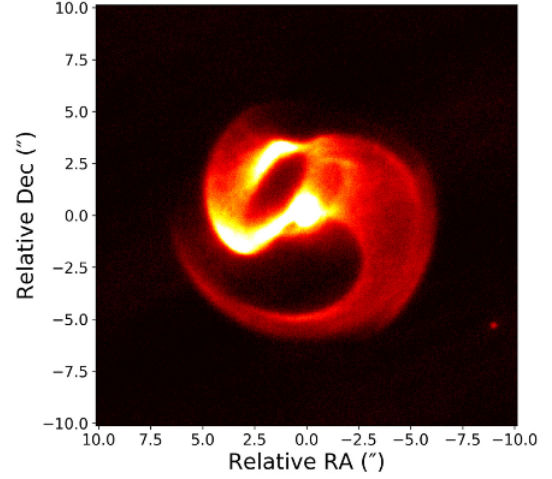


Figure 11. A reduced 8.9- μm image of Apep showing the dust pattern resembling the pinwheel nebulae (Han et al. 2020).

4 MODELLING THE NON-THERMAL EMISSION FROM APEP

Apep is a peculiar CWB system, as it consists of two WR stars, the first system of its kind to have been observed. It is the brightest and most luminous known non-thermal radio emitting CWB by over an order of magnitude (Marcote et al. 2020). This emission is likely produced by extremely powerful collisions between the strong WR winds. One of its most notable features is a spectacular expanding spiral dust plume, hundreds of AU across (shown in Fig. 11), likely formed as a result of the orbital motion. This structure has been likened to the pin-wheel nebulae. Apep is believed to be a strong progenitor candidate to a gamma-ray burst. The system is located around 2.4 kpc away from Earth, a larger distance compared to WR 147 (Del Palacio et al. 2022).

4.1 Parameters

To obtain a dependable set of initial parameters, various literature was consulted, as done with WR 147. The majority of the parameters were taken from (Del Palacio et al. 2022). These include the mass-loss rates, wind speeds, stellar temperatures, stellar radii, wind temperatures, filling factor, separation, distance, and inclination angle. The stars are identified by their spectral types, with the primary WR star referred to as the WN star whilst the secondary WR star is referred to as the WC star. Mass-loss rates were set to $\dot{M}_{WN} = 4.0 \times 10^{-5} M_\odot \text{ yr}^{-1}$ and $\dot{M}_{WC} = 2.9 \times 10^{-5} M_\odot \text{ yr}^{-1}$. While wind speeds of $v_{\infty WN} = 3.5 \times 10^9 \text{ cms}^{-1}$ and $v_{\infty WC} = 2.1 \times 10^9 \text{ cms}^{-1}$ were adopted. Stellar temperatures were set to $T_{WN} = 65000 \text{ K}$ and $T_{WC} = 60000 \text{ K}$. And stellar radii were set to $R_{WN} = 6.0 R_\odot$ and $R_{WC} = 6.3 R_\odot$. Using these values, luminosities of $L_{WN} = 5.79 \times 10^5 L_\odot$ and $L_{WC} = 4.63 \times 10^5 L_\odot$ were calculated. And wind temperatures of $T_{wind, WN} = 0.3 T_{WN}$ and $T_{wind, WC} = 0.3 T_{WC}$ were used. Abundance values of the WN star were set to the values previously obtained for the WR star in WR 147, due to similarity in spectral type between both stars. Thus, the WN abundances were set to $X = 0.09$, $Y = 0.89$, and $Z = 0.016$. As the secondary WR star in Apep is a WC star, WC abundances from the standard model described in section 2.2 were adopted, values of $X = 0$, $Y = 0.5$, and $Z = 0.5$. Initial values of the

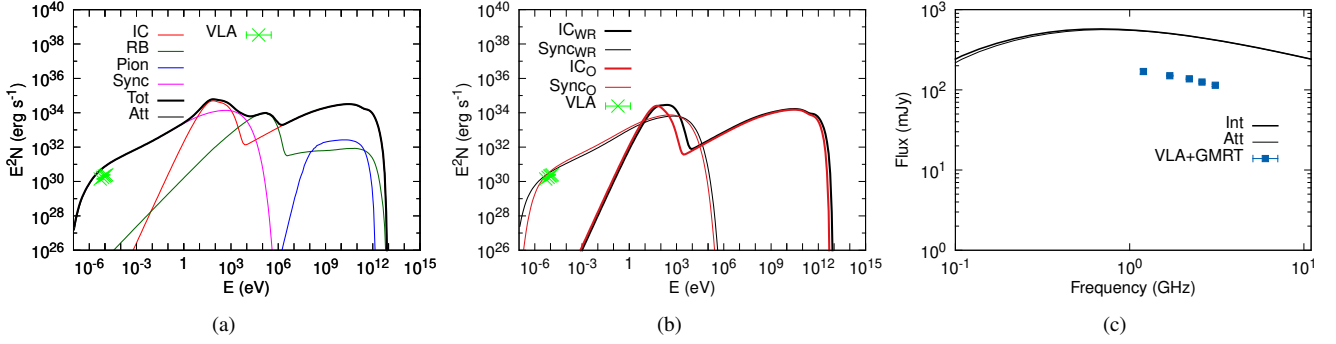


Figure 12. Model spectra for the initial model of Apep. (a) The model IC, relativistic bremsstrahlung, π^0 decay, synchrotron, total, and attenuated emission are shown with the observed radio data (labelled as "VLA"). (b) The IC and synchrotron emission from the particles accelerated at the WR (back lines) and O (red lines) shock. (c) The intrinsic and attenuated radio emission with the observed radio emission (labelled as "VLA+GMRT").

separation and inclination angle were set to $D_{sep} = 1.69 \times 10^{15} \text{ cm}$ and $\phi = 85^\circ$. To make adjustments to the separation accordingly after altering the inclination angle, the separation was calculated using $D_{sep} = 112.6 / \cos i \text{ AU}$, where $i = 90 - \phi$. And magnetic flux densities for both stars were again initially set to $B_* = 10 \text{ G}$ as a suitable starting point, as done with WR 147. And the filling factor was set to $f = 0.2$.

Using these initial parameters, model spectra were obtained, shown in Fig. 12. It can be seen from Fig 12a that the total non-thermal emission is a few orders of magnitudes stronger than what was apparent for WR 147. This is in line with the current understanding of Apep being a particularly luminous CWB. Key differences lie between this spectrum and the result for WR 147 (seen in Fig. 5a). As seen with WR 147, synchrotron emission dominates at $E \lesssim 1 \text{ eV}$. Unlike WR 147, the non-thermal emission from Apep is dominated by IC emission at two separate energy ranges, roughly between 10 and 100 eV at $E \gtrsim 10^6 \text{ eV}$. It can be assumed that the cause of the "bump" in the IC emission from both shocks (Fig. 12b) can be attributed to electrons undergoing downstream cooling, as was the case with WR 147. The "bump" in this case is significantly larger relative to the rest of the spectrum. It may be possible that in this instance, downstream cooling is more effective at altering the particle distribution than in the shocks generated in WR 147. The first instance of relativistic bremsstrahlung emission dominating is also observed, roughly between 10^4 and 10^6 eV . While the IC and relativistic bremsstrahlung appear stronger relative to the IC (compared to WR 147), the relative strength of the π^0 decay emission has reduced. At energies of $E \gtrsim 10^6 \text{ eV}$, relativistic bremsstrahlung emission becomes a few orders of magnitude weaker than the IC, commonly observed with WR 147. It can be seen in Fig. 12b that both stars make almost equivalent contributions to both the synchrotron and IC emission, which is somewhat expected as both stars have similar mass-loss rates, stellar radii and stellar temperatures. Fig. 12c displays the model radio spectrum compared to the observational radio data obtained from [Bloot et al. \(2022\)](#). As seen with WR 147 (Fig. 5c), there is a downturn in flux slightly below 1 Hz, which can again be attributed to a combination of the Razin effect and free-free absorption. And leading up to the turnover frequency the attenuation weakens, likely due to free-free absorption becoming negligible, as stated with WR 147. The initial parameters of Apep do not provide a good match for the observational radio data, suggesting that alterations need to be made in order to improve the fit.

4.2 Varying inclination angle and binary separation

Having obtained the initial model spectra ($\phi = 85^\circ$), plots were obtained for $\phi = 30^\circ$, and $\phi = 5^\circ$, corresponding to separation values of $D_{sep} = 3.37 \times 10^{15} \text{ cm}$ and $D_{sep} = 1.93 \times 10^{16} \text{ cm}$ respectively. Fig. 13 shows these results. The plots for $\phi = 30^\circ$ (Figs 12a, 12b, and 12c) appear somewhat similar to the results given by the initial value of $\phi = 85^\circ$. Synchrotron, IC, and relativistic bremsstrahlung dominate at similar energies whilst π^0 decay emission remains a few orders of magnitude weaker than the IC. There is no apparent change in the relative contribution to the synchrotron or IC emission from each shock, as seen in Fig. 12b. The radio plot also appears largely unchanged, thus it is not a good fit for the observational data.

Shown in Fig. 13d, Fig. 13e, and Fig. 13f) are the plots obtained for $\phi = 5^\circ$. It can be seen that synchrotron, IC, and relativistic bremsstrahlung emission dominate at the usual energies. While the plots appear similar in general structure to the initial results ($\phi = 85^\circ$), the total non-thermal emission (seen Fig. 13d) is visibly around an order of magnitude lower. This can be attributed to the change in binary separation which was increased as a result of lowering the inclination angle. Both shocks appear to make similar contributions to the synchrotron and IC emission, as previously observed for $\phi = 85^\circ$ and $\phi = 30^\circ$. The radio plot (Fig. 12f) appears more linear, this is likely due to the turnover frequency lowering and thus lying in a position below the minimum x-axis scale value. The model data appears to provide a fit which is nearly appropriate for the observational data, suggesting further tweaks may be required to achieve an acceptable fit.

Fig. 13g shows the total non-thermal emission for $\phi = 85^\circ$, $\phi = 30^\circ$, and $\phi = 5^\circ$ plotted together, while Fig. 13h shows the corresponding radio plots. The highest non-thermal emission is given by $\phi = 85^\circ$, followed by $\phi = 30^\circ$, and $\phi = 5^\circ$. The corresponding separation values in the same order are $D_{sep} = 1.69 \times 10^{15} \text{ cm}$, $D_{sep} = 3.37 \times 10^{15} \text{ cm}$, and $D_{sep} = 1.93 \times 10^{16} \text{ cm}$. As found with WR 147 (section 3.2), the total non-thermal emission scales inversely with binary separation across the majority of the spectrum. And similarly to WR 147, this relation can be attributed to the gas surrounding the WCR becoming more dense as both stars move closer together, resulting in an increased thermal energy density. Comparing Figs 13g and 7g, it is apparent that the non-thermal emission from Apep scales inversely with the separation across a wider energy range. It can be seen that at the lowest energies ($E \lesssim 10^{-6} \text{ eV}$), compared to the rest of the spectrum, the opposite trend occurs, as the non-thermal emission scales directly with separation. This

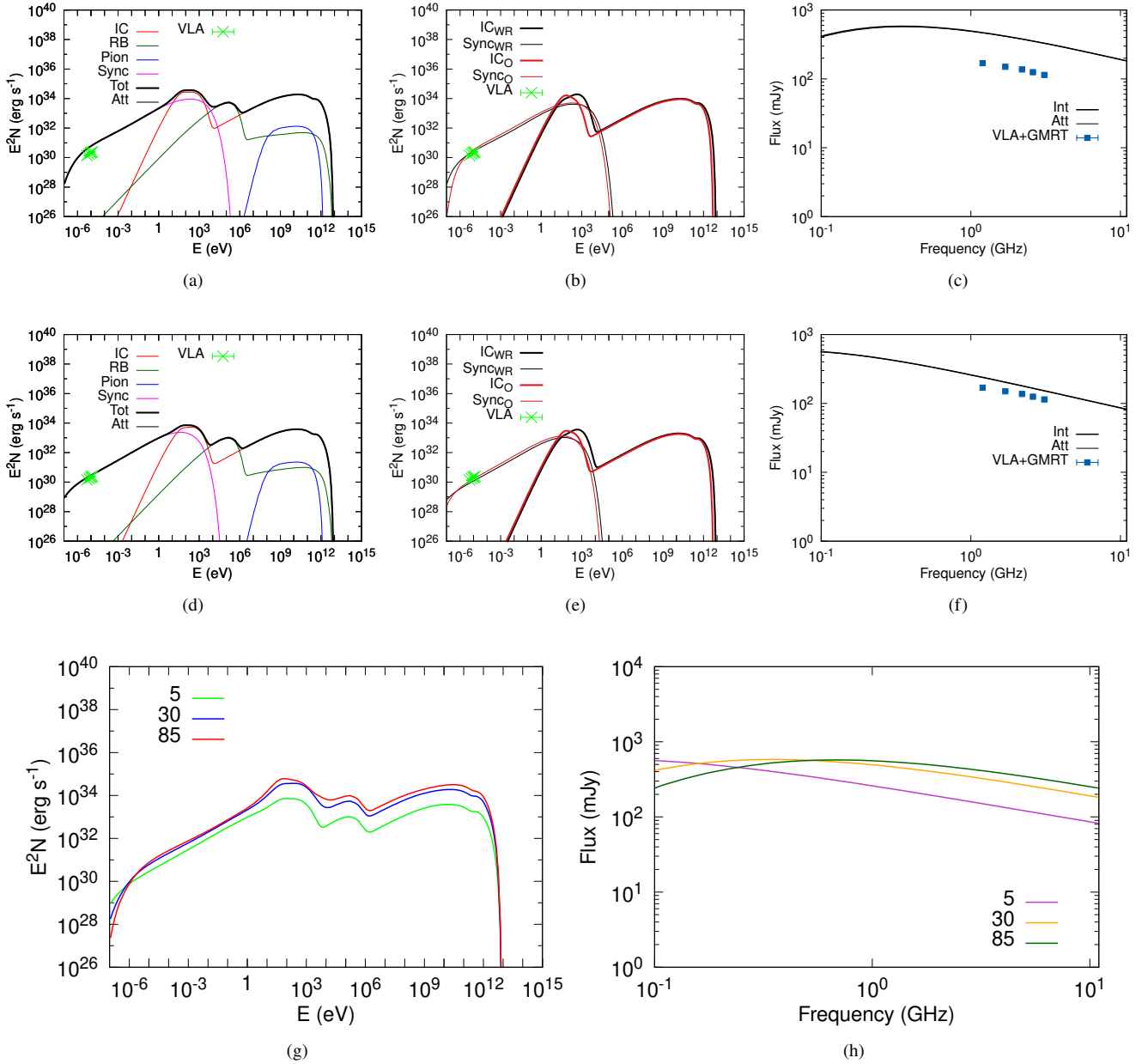


Figure 13. The dependence of the non-thermal emission on the inclination. Panels (a), (b), and (c) show the emission for $\phi = 30^\circ$ while panels (d), (e), and (f) represent the plots for $\phi = 5^\circ$. Panel (g) shows the total non-thermal emission for all three values of ϕ (including the initial value) while (h) exhibits the intrinsic radio emission for the same values.

is an outcome suggested as being viable in Pittard et al. (2006), where it was stated the cause is a combination of IC cooling, free-free absorption, and the Razin effect. To summarise, varying the separation of Apep yields the typical result of the non-thermal emission and turnover frequency scaling inversely with separation.

4.3 Varying the magnetic field

Fig. 14 shows the effect of adjusting magnetic flux density on the resulting non-thermal emission. Shown in Fig. 14a, Fig. 14b, and Fig. 14c are the emission plots for the magnetic flux density of both stars set to $B_* = 1G$. From Fig. 14a, it can be seen that synchrotron

dominates at $E \lesssim 0.1$ eV, a slight reduction in range compared to the initial plot ($B_* = 10G$) where it dominates up to 1 eV. The synchrotron emission has also reduced by around two orders of magnitude. IC emission continues to dominate at similar energies to what was observed in the initial plot. And relativistic bremsstrahlung emission dominates roughly between 10^4 and 10^6 eV as previously seen for the initial plot. There is no clear change in the π^0 decay emission, as it remains a few orders of magnitude weaker than the IC. Further likeness is observed in Fig. 14b, which appears unaltered in comparison to the initial plot (Fig. 12b). Both shocks continue to make similar contributions to the synchrotron and IC emission. The radio emission (Fig. 14c) is roughly an order of magnitude weaker

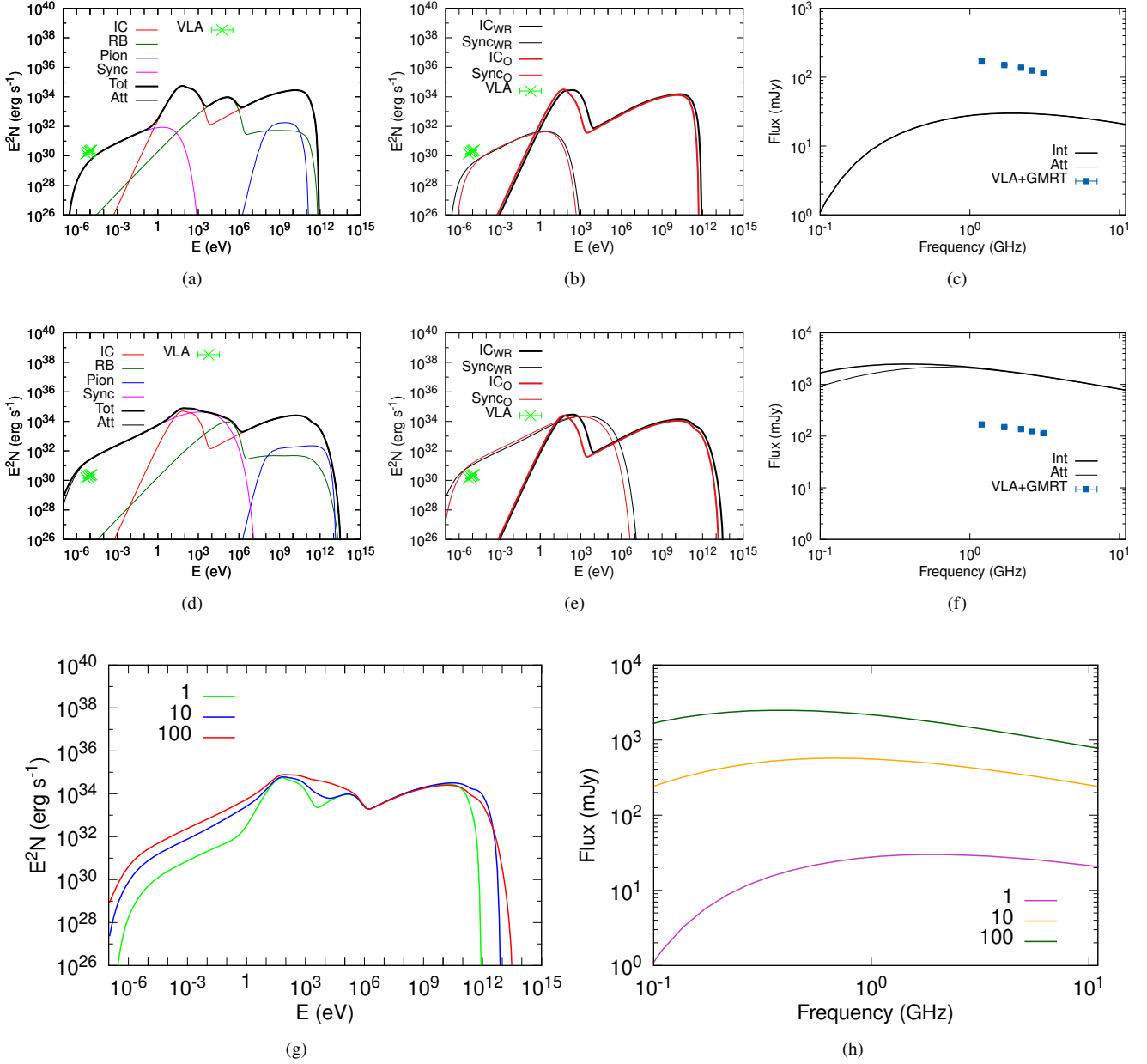


Figure 14. The dependence of the non-thermal emission on the magnetic flux density. Panels (a), (b), and (c) show the emission for $B_* = 1G$ while panels (d), (e), and (f) represent the plots for $B_* = 100G$. Panel (g) shows the total non-thermal emission for all three values of B_* (including the initial value) while (h) exhibits the intrinsic radio emission for the same values.

than seen in Fig. 12c. The plot shows that the model emission is too low to be a good fit for the observational data by approximately an order of magnitude.

Shown in Fig. 14d, Fig. 14e, and Fig. 14f are the plots for $B_* = 100G$. The general structure appears somewhat similar to what was seen in the initial plot (Fig. 12a). From Fig. 14d, it can be seen the synchrotron emissions is marginally stronger (less than an order of magnitude) between 100 and 10^5 eV. Due to the increase in strength of synchrotron emission in the lower energies, IC emission now only clearly dominates at $E \gtrsim 10^6$ eV. Another consequence of this increase is that there is no notable region where relativistic bremsstrahlung emission is dominant. The π^0 decay

emission remains a few orders of magnitude fainter than the IC. The contribution of each star's shock to the synchrotron and IC emission (Fig. 14e) remains somewhat equal, compared to the initial plot (Fig. 12b). The radio plot (Fig. 14f) shows that the model radio emission is too strong to be a good fit for the observational data.

The total non-thermal emission for $B_* = 1G$, $B_* = 10G$, and $B_* = 100G$ is plotted together in Fig. 14g, with the corresponding intrinsic radio data being plotted in Fig. 14h. Until the higher energies ($E \lesssim 10^5$ eV), the non-thermal emission appears to strengthen as B_* is increased. Between 10^5 and 10^{10} eV, adjusting the flux density has no impact on the emission. And at the rest of the spectrum ($E \gtrsim 10^{10}$ eV), a complex scaling is evident, as generally

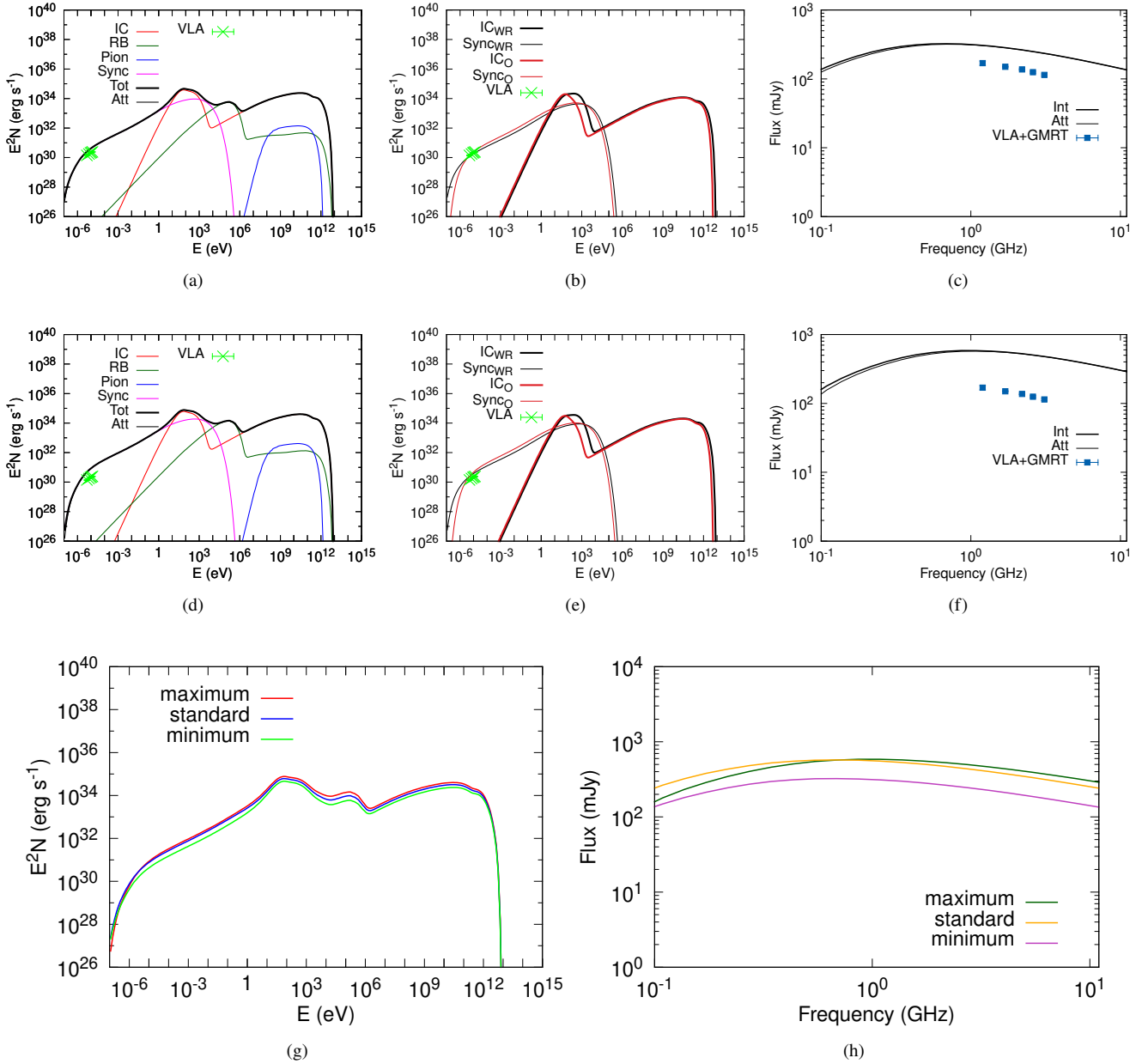


Figure 15. The dependence of the non-thermal emission on the mass-loss rate. Panels (a), (b), and (c) show the emission for $\dot{M}_{WN} = 3.0 \times 10^{-5} M_{\odot} \text{yr}^{-1}$ and $\dot{M}_{WC} = 2.2 \times 10^{-5} M_{\odot} \text{yr}^{-1}$ while panels (d), (e), and (f) represent the plots for $\dot{M}_{WN} = 5.0 \times 10^{-5} M_{\odot} \text{yr}^{-1}$ and $\dot{M}_{WC} = 3.7 \times 10^{-5} M_{\odot} \text{yr}^{-1}$. Panel (g) shows the total non-thermal emission for all three models (including the standard mass-loss rate) while (h) exhibits the intrinsic radio emission for the same values.

seen with WR 147 (section 3.3). Figs 12a, 14a, and 14d show that relative to the other processes, synchrotron emission scales effectively with B_* . The other processes not scaling notably with B_* is what results in the total non-thermal emission only increasing with the flux density at lower energies. As the magnetic field increases, at lower energies the particle acceleration efficiency at both shocks improves with the increase in the Alfvénic Mach number. As a result, synchrotron emission strengthens. In this instance, a reduction in particle acceleration efficiency triggered by Alfvén wave heating is not apparent. However, it is likely that these conflicting processes play a role in the higher energy emission (mainly IC cooling). In

section 3.3, it was established that synchrotron emission from a WR shock scales directly with B_* , which was attributed to the WR shock residing further from the WR star. The modelling of Apep reveals that the synchrotron emission from both WR shocks in Apep also scales directly with B_* . As the WN and WC stars have somewhat equal strength winds, it is a possibility the WCR lies closer to midway between both stars compared to a typical CWB, with both shocks residing relatively far from their stars. This may be the reasoning for the same resulting outcome as section 3.3. Contrast lies in the turnover frequency, which is found to increase with a weaker magnetic field, which is consistent with Pittard et al. (2021).

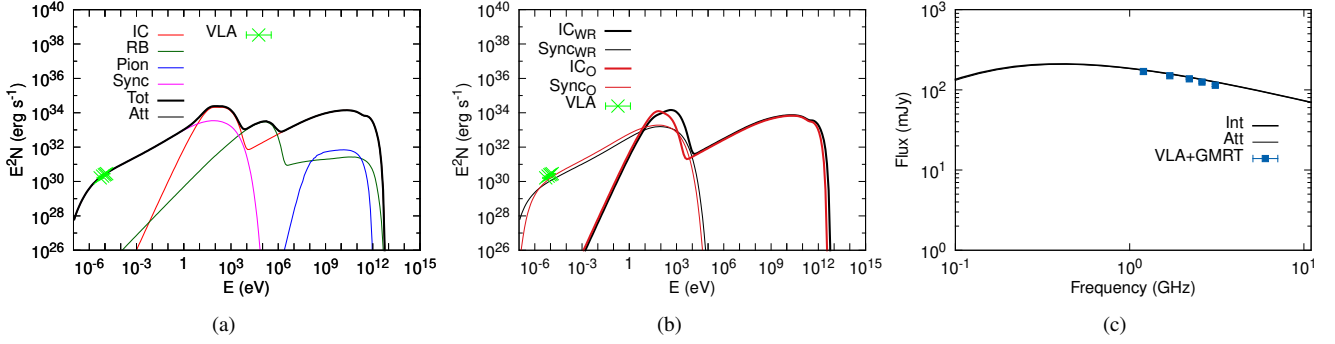


Figure 16. The model spectra for the final model of Apep.

An appropriate fit for the observational data remains to be found. To conclude, the lower energy non-thermal emission scales directly with the magnetic flux density whilst at higher energy the dependency is more complex.

4.4 Varying mass-loss rate

Fig. 15 shows the effect of adjusting the mass-loss rates of both stars. Plots were made for the minimum and maximum mass-loss rates taken from Del Palacio et al. (2022). Shown in Fig. 15a, Fig. 15b, and Fig. 15c are the emission plots for the minimum mass-loss rates, set to $\dot{M}_{WN} = 3.0 \times 10^{-5} M_{\odot} \text{yr}^{-1}$ and $\dot{M}_{WC} = 2.2 \times 10^{-5} M_{\odot} \text{yr}^{-1}$. It can be seen in Fig. 15a that synchrotron emission dominates at $E \lesssim 1$ eV. IC emission dominates roughly between 10 and 100 eV as well as at $E \gtrsim 10^6$ eV, as seen initially in Fig. 12a. Similarity also lies in the relativistic bremsstrahlung emission, which continues to dominate loosely between 10^4 and 10^6 eV. The π^0 decay emission also appears relatively unchanged, as it remains a few orders of magnitude weaker than the IC. There are further parallels in Fig. 15b, and Fig. 15c, which resemble their counterparts from Fig. 12. Both shocks appear to make almost equivalent contributions to both the synchrotron and IC emission (an unchanged outcome compared to Fig. 12b), and the model radio emission remains too strong for the observational data, and thus not a good fit.

Shown in Fig. 15d, Fig. 15e, and Fig. 15f are plots for the maximum mass-loss rates, set to $\dot{M}_{WN} = 5.0 \times 10^{-5} M_{\odot} \text{yr}^{-1}$ and $\dot{M}_{WC} = 3.7 \times 10^{-5} M_{\odot} \text{yr}^{-1}$. The plots appear to bear a strong resemblance to the initial results (Fig. 12a). Synchrotron, IC, and relativistic bremsstrahlung dominate at the usual energies, and π^0 decay emission remains a few orders of magnitude weaker than the IC. As seen with the standard and maximum mass-loss rates, the shocks make very comparable contributions to the synchrotron and IC emission. And the model radio emission remains too strong for the observational data, thus a good fit is not achieved.

In Fig. 15g, the total non-thermal emission for the minimum, standard, and maximum mass-loss rates are plotted together, with the corresponding radio data being plotted in Fig. 15h. The highest non-thermal emission is given by the maximum mass-loss rate, followed by the standard, and minimum values. It is clear that the non-thermal emission scales directly with the mass-loss rate, an expected outcome which was also observed with WR 147. The scaling in this case is more subtle, likely due to the lower range of mass-loss rates used for the modelling. As previously explained in section 3.4, a higher mass-loss rate naturally provides a greater amount of energy in the WCR for particle acceleration to occur and non-thermal emission to be produced. It is apparent that at lower

energies free-free absorption and the Razin effect do not have a notable influence in either shock, an outcome previously seen with a varying O mass-loss rate for WR 147 (section 3.5). All emission processes appear to scale with the mass-loss rate to a similar degree. The larger population of non-thermal electrons results in stronger relativistic bremsstrahlung emission and the higher frequency of hadronic collisions increases the π^0 decay emission. While the relation is subtle, from Fig. 15h, it can be deduced that increasing the mass-loss rates increases the turnover frequency (as expected and previously found in section 3.4 and 3.5). An acceptable fit for the observational radio data remains yet to be achieved with any of the aforementioned values.

4.5 Final model

Unlike WR 147, a number of parameters were adjusted in order to achieve an appropriate fit for the observational radio data. The inclination angle, binary separation, magnetic flux densities and mass-loss rates were all altered from their original values mentioned in section 4.1. An inclination angle of $\phi = 30^\circ$ was adopted, which in turn gave a separation of $D_{sep} = 3.37 \times 10^{15}$. Magnetic fields were set to $B_* = 7G$ for both stars. And mass-loss rates were assigned to their minimum values of $\dot{M}_{WN} = 3.0 \times 10^{-5} M_{\odot} \text{yr}^{-1}$ and $\dot{M}_{WC} = 2.2 \times 10^{-5} M_{\odot} \text{yr}^{-1}$. The distance was also set to its maximum value of 2.6 kpc (also retrieved from Del Palacio et al. (2022)) as part of further efforts to lower the radio emission to an acceptable value. Reasonable adjustments were made to most parameters with the exception of the inclination angle and the resulting binary separation. While the inclination angle and binary separation are notably different compared to the initial values taken from the literature, the alteration may still be considered somewhat acceptable as Apep and most CWB systems do not have particularly well constrained parameters. Thus, this allows the parameters some room for deviation from values quoted from publications. The emission plots of the final model can be seen in Fig. 16. As seen with the initial model (Fig. 12a), synchrotron emission dominates at $E \lesssim 1$ eV. The lower energy region where the IC emission dominates is marginally wider in the final model, dominating between 10 and 1000 eV compared to the initially observed range of between 10 and 100 eV, and also at the unchanged range of $E \gtrsim 10^6$. Relativistic bremsstrahlung emission continues to dominate between 10^4 and 10^6 eV, whilst π^0 decay emission remains a few orders of magnitude weaker than the IC. And from Fig. 16b, it is evident both shocks make more or less equivalent contributions to both the synchrotron and IC emission, an unchanged outcome from the initial model. Fig. 16c

Table 3. The parameters used in the final model of Apep. An inclination angle of $\phi = 30^\circ$ implies a binary separation of $D_{sep} = 3.37 \times 10^{15} \text{ cm}$. And the distance is set to 2.6 kpc.

Parameter	WR star	O star
$\dot{M} (M_\odot \text{ yr}^{-1})$	3×10^{-5}	2.2×10^{-5}
$v_\infty (kms^{-1})$	35 000	21 000
$L (L_\odot)$	5.79×10^5	4.63×10^4
$T_{eff} (K)$	65 800	60 000
$R_* (R_\odot)$	6.0	6.3
$T_{wind} (K)$	1 950	1 800
X	0.09	0
Y	0.89	0.5
Z	0.016	0.5
$B_* (G)$	7	7
v_{rot}/v_∞	0.1	0.1
f	0.2	0.2

shows the model radio emission providing an excellent fit for the observational data.

4.6 Apep summary

As with WR 147, various parameters were adjusted to investigate the effect they have on the non-thermal emission. The total non-thermal emission and turnover frequency are found to scale inversely with the separation, an expected outcome for a CWB system. It is found that at higher energies ($E \gtrsim 10^{10} \text{ eV}$), the non-thermal emission scales in a complex manner with B_* , as a result of conflicting processes in the WCR. The synchrotron emission at both shocks is the only emission process which appears to directly scale with B_* . And the turnover frequency has an inverse relation with B_* . Varying the non-thermal emission also yielded an expected outcome. The total non-thermal emission is found to increase with a higher mass-loss rate, due to the greater amount of energy available in the WCR. The turnover frequency also scales directly with the mass-loss rate. In the final model a number of parameters from the initial model are altered. The final model parameters of Apep are listed in Table 3.

5 CONCLUSIONS

A recently developed numerical model is applied on the CWB systems WR 147, one of the widest known CWBs, and Apep, the brightest non-thermal radio emitting CWB. Both systems represent an opportunity to investigate the scaling of the non-thermal emission with various parameters as they are altered. Reducing binary separation results in stronger emission and a higher turnover frequency for both systems, this relation is the expected outcome for CWBs. Contrast lies in the π^0 decay emission from WR 147, which was found to particularly benefit from a reduced separation. This was not observed with Apep. Further dissimilarity between both systems lies with the adjustment of the magnetic flux density. While the non-thermal emission from WR 147 was found to scale in a complex manner, this scaling was only applicable for Apep at higher energies ($E \gtrsim 10^{10} \text{ eV}$). Turnover frequency has an inverse relation with B_* in Apep, which is typically expected, but not WR 147. A higher value of B_* strengthened the π^0 decay emission from WR 147 relative to the other processes, but the corresponding emission spectrum from Apep is only widened, with the peak flux remaining relatively unchanged. With both systems, it is found that a higher mass-loss rate increases

both the total non-thermal emission as well as the turnover frequency. In order to provide a good fit for the observational radio data, the parameters of Apep required more adjustment in comparison to WR 147, but most alterations were to an acceptable degree. To conclude the findings, the results of modelling the non-thermal emission from WR 147 and Apep are presented, with a range of parameters adjusted for each system to investigate the effects. The presented findings are generally consistent with background knowledge as well various publications where similar modelling is carried out.

6 FURTHER WORK

Having applied the model on a WR+O and WR+WR system, the opportunity remains to carry out similar modelling of an O+O binary. An example of such a system is Cyg OB2 No. 5, a wide binary consisting of two supergiant stars (Kennedy et al. 2010). Modelling can also be carried out for systems with less well constrained parameters such as WR 140 (the prototypical WR+O CWB (Pittard 2009)), Eta Carinae (a particularly luminous CWB (Gull et al. 2011)), and Cyg OB2 No. 8A (one of the optically brightest O+O CWBs (De Becker et al. 2004)). As improved iterations of such models are applied on a growing variety of CWBs, the current knowledge of particle acceleration and non-thermal emission in such environments is destined to expand.

ACKNOWLEDGEMENTS

Special thanks goes to Dr Julian Pittard for his supervision, assistance, and encouragement throughout the project.

REFERENCES

- Badala A., Barbera R., Palmeri A., Pappalardo G. S., Riggi F., Russo A. C., Russo G., Turrisi R., 1994, *Nucl. Instrum. Meth. A*, 350, 192
- Baring M. G., 1997, in 32nd Rencontres de Moriond: High-Energy Phenomena in Astrophysics. p. 97
- Bloot S., Callingham J. R., Marcote B., 2022, *Monthly Notices of the Royal Astronomical Society*, 509, 475
- Churchwell E., Biegging J. H., van der Hucht K. A., Williams P. M., Spoelstra T. A. T., Abbott D. C., 1992, *The Astrophysical Journal*, 393, 329
- Contreras M. E., Rodriguez L. F., 1999, *The Astrophysical Journal*, 515, 762
- Crowther P. A., 2007, *Annual Review of Astronomy and Astrophysics*, 45, 177
- De Becker M., Rauw G., Manfroid J., 2004, *Astronomy & Astrophysics*, 424, L39
- Del Palacio S., Benaglia P., De Becker M., Bosch-Ramon V., Romero G. E., 2022, *Publications of the Astronomical Society of Australia*, 39
- Dougherty S. M., Pittard J. M., Kasian L., Coker R. F., Williams P. M., Lloyd H. M., 2003, *Astronomy & Astrophysics*, 409, 217
- Ellison D. C., Decourchelle A., Ballet J., 2004, *Astronomy & Astrophysics*, 413, 189
- Eriksson S., Rastätter L., 2013, *Geophysical Research Letters*, 40, 1257
- Grieder P., 2001, Cosmic Ray Properties, Relations and Definitions. p. 1
- Gulkis S., de Pater I., 2003, in Meyers R. A., ed., , *Encyclopedia of Physical Science and Technology* (Third Edition), third edn, Academic Press, New York, p. 687
- Gull T. R., Madura T. I., Groh J. H., Corcoran M. F., 2011, *The Astrophysical Journal Letters*, 743, L3
- Hamann W.-R., Graefener G., Liermann A., 2006, *Astronomy & Astrophysics*, 457, 1015
- Han Y., et al., 2020, *Monthly Notices of the Royal Astronomical Society*, 498, 5604

- Kennedy M., Dougherty S. M., Fink A., Williams P. M., 2010, *The Astrophysical Journal*, 709, 632
- Kroupa P., 2004, *New Astronomy Reviews*, 48, 47
- Lee M., 1996, *Space Science Reviews*, 78, 109
- Marcote B., Callingham J. R., Becker M. D., Edwards P. G., Han Y., Schulz R., Stevens J., Tuthill P. G., 2020, *Monthly Notices of the Royal Astronomical Society*, 501, 2478
- Moran J. P., Davis R. J., Bode M. F., Taylor A. R., Spencer R. E., Argue A. N., Irwin M. J., Shanklin J. D., 1989, *Nature*, 340, 449
- Pittard J. M., 2009, *Monthly Notices of the Royal Astronomical Society*, 396, 1743
- Pittard J. M., 2010, *Monthly Notices of the Royal Astronomical Society*, 403, 1633
- Pittard J. M., Dougherty S. M., 2006, *Monthly Notices of the Royal Astronomical Society*, 372, 801
- Pittard J. M., Parkin E. R., 2010, *Monthly Notices of the Royal Astronomical Society*, 403, 1657
- Pittard J. M., Dougherty S. M., Coker R. F., O'Connor E., Bolingbroke N. J., 2006, *Astronomy & Astrophysics*, 446, 1001
- Pittard J. M., Vila G. S., Romero G. E., 2020, *Monthly Notices of the Royal Astronomical Society*, 495, 2205
- Pittard J. M., Romero G. E., Vila G. S., 2021, *Monthly Notices of the Royal Astronomical Society*, 504, 4204
- Silaj J., Jones C. E., Sigut T. A. A., Tycner C., 2014, *The Astrophysical Journal*, 795, 82
- Stacy J., Vestrand W., 2003, in Meyers R. A., ed., , Encyclopedia of Physical Science and Technology (Third Edition), third edn, Academic Press, New York, p. 397
- Stevens I. R., Blondin J. M., Pollock A., 1992, *The Astrophysical Journal*, 386, 265
- Vink J., Yamazaki R., 2014, *The Astrophysical Journal*, 780, 125
- Williams P. M., Dougherty S. M., Davis R. J., Hucht K. A., Bode M. F., Gunawan D., 1997, *Monthly Notices of the Royal Astronomical Society*, 289, 10

APPENDIX A: CWB STRUCTURE

The intersection of contact of the winds in a CWB system can be found using the one dimensional momentum balance, which states

$$\rho_1 v_1^2 = \rho_2 v_2^2 \quad (\text{A1})$$

where v_1 and v_2 are the constant terminal wind velocities, and ρ_1 and ρ_2 are the corresponding momentum values. Using this equation gives

$$R = \left(\frac{\dot{M}_1 v_1}{\dot{M}_2 v_2} \right)^{\frac{1}{2}} = \frac{d_1}{d_2} \quad (\text{A2})$$

Where R is the wind momentum ratio, \dot{M}_1 and \dot{M}_2 are the mass-loss rates, and d_1 and d_2 are the distances of each star from its shock. The contact discontinuity lies along the surface of momentum balance when $R = 1$ (Churchwell et al. 1992).

APPENDIX B: THE RAZIN EFFECT

As a charged particle (such as an electron) travels closer to the speed of light, the angle between photons emanating from that particle and the particle's direction of motion will get narrower, this is referred to as relativistic beaming. Relativistic charges surrounded by a plasma will have this beaming effect suppressed. This effect is approximated as a reduction in flux at a cut-off frequency which is given by

$$\nu_R \approx 20 \frac{n_e}{B} \quad (\text{B1})$$

where ν_R is the Razin turnover frequency, n_e is the electron number density, and B is the magnetic flux density (Pittard et al. 2006).

APPENDIX C: ALFVÉN MACH NUMBER

The Alfvén Mach number characterises the strength of a magnetic field. It is given by

$$M_A = \frac{V}{V_A} \quad (\text{C1})$$

where M_A is the Alfvén Mach number of the shock, V is the shock speed, and V_A is the Alfvén speed. The Alfvén speed is given by

$$V_A = \frac{B}{\sqrt{\mu_0 m_p N}} \quad (\text{C2})$$

where B is the magnetic flux density, μ_0 is the permeability of free space, m_p is the proton mass, and N is the proton number density (Eriksson & Rastätter 2013).